AGU PUBLICATIONS

JGR

Journal of Geophysical Research: Atmospheres

RESEARCH ARTICLE
10.1002/2016JD025660

Key Points:
- The distributions of the hygroscopic growth factor of aerosol particles were unimodal
- Hygroscopicity parameter κ of newly formed particles was 0.12–0.16
- CCN and cloud droplet activation can be greatly influenced by new particle formation

Supporting Information:
- Supporting Information S1

Correspondence to:
M. Mochida,
mochida.michihiro@g.mbox.nagoya-u.ac.jp

Citation:
Kawana, K., T. Nakayama, N. Kuba, and M. Mochida (2017), Hygroscopicity and cloud condensation nucleus activity of forest aerosol particles during summer in Wakayama, Japan, *J. Geophys. Res. Atmos.*, *122*, 3042–3064, doi:10.1002/2016JD025660.

Received 16 JUL 2016
Accepted 20 FEB 2017
Accepted article online 22 FEB 2017
Published online 15 MAR 2017

Hygroscopicity and cloud condensation nucleus activity of forest aerosol particles during summer in Wakayama, Japan

Kaori Kawana[1,2], Tomoki Nakayama[3,4], Naomi Kuba[5], and Michihiro Mochida[1]

[1]Department of Earth and Environmental Science, Graduate School of Environmental Studies, Nagoya University, Nagoya, Japan, [2]Now at Department of Basic Science, Graduate School of Arts and Sciences, University of Tokyo, Tokyo, Japan, [3]Solar-Terrestrial Environment Laboratory, Nagoya University, Nagoya, Japan, [4]Now at Institute for Space-Earth Environmental Research, Nagoya University, Nagoya, Japan, [5]Atmosphere and Ocean Research Institute, University of Tokyo, Kashiwa, Japan

Abstract Size-resolved distributions of the hygroscopic growth factor (g) and the ratios of cloud condensation nuclei (CCN) to condensation nuclei were observed at a forest site during summer in Japan. The g distributions at 85% relative humidity were unimodal. During 0900–2100 Japan Standard Time (JST) on new particle formation (NPF) event days, less hygroscopic particles ($g \sim 1.1$) were dominant in the Aitken-mode range and the CCN activation diameters of the aerosols were large. These results are explained by the substantial contribution from newly formed biogenic secondary organic aerosol (BSOA). Hygroscopicity parameter κ for newly formed Aitken particles, calculated from g and CCN activation diameters, were 0.12 and 0.16, respectively, which were estimated to be the κ of organics. The κ values of particles were higher during 2100–0900 JST on NPF event days, in which the aerosols were characterized by the dominance of large and more hygroscopic particles. The number fractions of CCN that were predicted from time- and size-resolved g at 0.23% and 0.41% supersaturations better matched the measured values compared to the cases with the time-averaged g and/or g for the bulk composition, which suggests that the differences in particle hygroscopicity with time and size are important to CCN activation. A cloud parcel model indicates that the contributions from less hygroscopic particles to the number concentrations of CCN and cloud droplets were potentially large during NPF event days, which suggests a marked contribution from locally formed BSOA particles alongside particles from background air.

1. Introduction

Forests constitute a portion of the Earth's ecosystem and play an important role in the atmosphere as a main source of biogenic secondary organic aerosol (BSOA) particles, which are formed through the photochemical oxidation of biogenic volatility organic compounds (BVOCs). The formation of BSOA from BVOCs and their growth to cloud condensation nuclei (CCN) and cloud droplets are important for the climate [*Kulmala et al.,* 2004; *Andreae and Rosenfeld,* 2008; *Pöschl et al.,* 2010; *Martin et al.,* 2010]. To understand the role of BSOA, it is important to analyze the relationship between BSOA and CCN (i.e., their contribution to CCN number concentrations (N_{CCN})) as well as the temporal and spatial variations in BSOA and CCN in the atmosphere. Field observations as well as laboratory experiments and modeling studies are required to achieve this objective.

The CCN activity of aerosol particles is governed by both the particle size and the hygroscopicity, which is regulated by the chemical composition. (Here the term "hygroscopicity" represents the solute (Raoult) effect, and the term "CCN activity" represents the combination of the solute and surface tension (Kelvin) effects.) Therefore, the relationship among the size, hygroscopicity, and composition is a key factor in understanding the behavior and role of BSOA particles in forest environments. The hygroscopicity of particles under subsaturated conditions is investigated using a hygroscopicity tandem differential mobility analyzer (HTDMA), which provides the hygroscopic growth factor (g) distributions of the particles. Moreover, the CCN activation of particles, i.e., particle hygroscopic growth under supersaturated conditions is investigated using a CCN counter (CCNC). Although the hygroscopicity and CCN activity of particles formed from BVOC precursor gases under different conditions have been reported from laboratory experiments (e.g., g of ~1.1 and hygroscopicity parameter (κ) of ~0.1) [*VanReken et al.,* 2005; *Huff Hartz et al.,* 2005; *Varutbangkul et al.,* 2006; *Engelhart*

et al., 2008, 2011; *Lang-Yona et al.,* 2010], the association to ambient BSOA is not necessarily warranted because multiple precursors and oxidants should contribute to BSOA formation simultaneously, depending on the local vegetation and inflows of anthropogenic plumes.

Based on field observations, the κ values of forest aerosol particles or their CCN-activated particles have been determined to be 0.1–0.2 [*Gunthe et al.,* 2009; *Dusek et al.,* 2010; *Cerully et al.,* 2011; *Sihto et al.,* 2011; *Levin et al.,* 2014]. Because the composition of BSOA should depend on precursor BVOCs and thus the vegetation that emits them, investigating the hygroscopicity of particles and organics in different environments is important. The hygroscopicity and BSOA should depend on the degree of aging [*Huff Hartz et al.,* 2005; *VanReken et al.,* 2005; *Cerully et al.,* 2011], so characterizing the hygroscopicity of BSOA with information regarding when they are formed in the atmosphere is important.

Some studies have shown that the properties of forest aerosols are strongly influenced by new particle formation (NPF) events. Frequent NPF events have been observed in some forest sites, e.g., in the boreal forest site of Hyytiälä, northern Europe. Additionally, newly formed particles contribute greatly to the increase in the mass and number concentrations of aerosol particles (N_{CN}) and N_{CCN} [*Tunved et al.,* 2006; *Riipinen et al.,* 2011]. *Sihto et al.* [2011] reported that newly formed particles contributed to a 70%–110% increase in N_{CCN} based on atmospheric observation, compared with those during nonevent days. Previous studies based on atmospheric observations have shown that particles formed by nucleation grew rapidly via the condensation of sulfuric acid and organic vapors, which accompanied changes in particle size, particle hygroscopicity, and CCN activity [*Hämeri et al.,* 2001; *Kulmala et al.,* 2001; *Boy et al.,* 2004; *Ehn et al.,* 2007]. Because the contributions from newly formed particles to N_{CCN} have been estimated to be substantial on a global scale (5%–60%) [*Spracklen et al.,* 2008; *Merikanto et al.,* 2009; *Wang and Penner,* 2009; *Yu and Luo,* 2009], it is important to clarify the relationship between the hygroscopicity/CCN activity of aerosols and new particle formation under different forest environments. However, field-based forest aerosol studies were not thoroughly performed for a wide range of regions, and there have been few reports on the hygroscopicity, CCN activity, and chemical composition of aerosol particles and newly formed BSOA in Asia [*Irwin et al.,* 2011; *Miyazaki et al.,* 2012; *Jung et al.,* 2013]. To our knowledge, no reports have been published on the hygroscopicity and CCN activity of BSOA in relation to the formation of new particles in Asian forests and their contribution to N_{CCN}.

In this study, the *g* distributions at 85% relative humidity (RH) and the ratios of CCN to aerosol particles (CN) were measured at a forest site in Wakayama, Japan, in August 2010. The variations in the size- and time-resolved *g* distributions and the CCN activity of forest aerosol particles were observed using an HTDMA and a CCNC on days with and without NPF events. The κ values of the forest aerosols were calculated from both the HTDMA and CCNC data and compared to assess the particle hygroscopicity under subsaturated and supersaturated conditions. Moreover, the κ values of locally formed fresh organics (κ_{org}) were calculated from the particle hygroscopicity and chemical composition and compared with the values in different forest environments and from laboratory studies. The N_{CCN}/N_{CN} ratios were predicted based on the *g* distributions and compared with the measured values to investigate the appropriateness of the estimate of CCN number concentrations from the particle hygroscopicity under subsaturated conditions. Furthermore, N_{CD} and the effective radii of cloud droplets (R_{eff}) after cloud formation were predicted using a cloud parcel model with inputs from size-resolved *g* distributions. The contributions of BSOA and newly formed particles to cloud droplet formation are discussed.

2. Experiment

2.1. Measurements

Atmospheric aerosols were observed from 0600 Japan Standard Time (JST) on 20 August 2010 to 0600 JST on 30 August 2010 at the Wakayama Forest Research Station of Kyoto University (34.06°N, 135.52°E), located at a midlatitude forest site on the Kii Peninsula, Japan. The observation site is ~500 m above sea level. The area around the site is covered by both coniferous and broadleaf tree species (e.g., *Cryptomeria japonica* and *Chamaecyparis obtusa* plantation, and *Quercus crispula*, *Quercus serrata*, and *Pinus densiflora* communities) [*Okumura,* 2009]. The mean (range) air temperature, RH, and solar radiation during the observation were 23.1 (18.5–30.0)°C, 92.8% (62.5%–99.1%), and 0.15 (0–0.97) kW m^{-2}, respectively. The emissions of isoprene, monoterpenes, and sesquiterpenes from the area with these tree species were extracted from emission studies [*Tani and Kawawata,* 2008; *Mochizuki et al.,* 2011; *Matsunaga et al.,* 2011;

Matsunaga et al., 2013]. *Ramasamy et al.* [2016] reported the presence of these VOCs at the site based on the observation during summer in a different year. They reported similar average mixing ratios of isoprene and the sum of 12 monoterpenes.

An HTDMA coupled to a CCN counter (CCNC, Droplet Measurement Technologies, USA) was operated in parallel with a scanning mobility particle sizer (SMPS, model 3080, 3081, and 3772, TSI, USA). The configuration of the HTDMA-CCNC system and the SMPS was the same as that shown in Figure 1 of *Kawana et al.* [2016]. The inlet for aerosol sampling was placed 7.5 m from the ground. Atmospheric aerosol particles aspirated from the inlet were passed through a PM_1 cyclone (flow rate: 16.7 L min^{-1}, URG-2000-30EHB, URG, USA). After drying using two diffusion driers filled with silica gel and a molecular sieve, the aerosol particles were introduced to the HTDMA-CCNC system. The particles (RH < 2%) in the aerosols were classified with a specific $d_{p,dry}$ at 24.1–359 nm by a first differential mobility analyzer (DMA) (DMA1, model 3080, TSI, USA) in the HTDMA. The classified aerosols were humidified by passing through Nafion tubing (model MD-110-24S-4, Perma Pure) and introduced to a second DMA (DMA2, model 3080, 3081, TSI, USA) coupled to a condensation particle counter (CPC) (CPC1, model 3775, TSI, USA) to obtain size-resolved g distributions at ~85% RH. During the measurements including those for calibration, the RHs at the sample-air inlet and the sheath-air inlet of DMA2 were 85.0% ± 1.4% and 85.2% ± 1.4%, respectively (the uncertainty of the RH sensors was considered). The residence time of the particles in the HTDMA from the humidifier to the inlet of DMA2 was estimated to be ~12 s. The particles that were selected in DMA1 were also introduced to the CCNC and another CPC (CPC2, model 3025A, TSI, USA) to obtain the size-resolved CCN/CN ratios. The diameter setting of DMA1 was changed to a time resolution of 5 min, and one cycle of HTDMA-CCNC measurement for 34 sizes at 24.1–359 nm was 3 h. The ratios of the sheath to sample flow rates for the DMAs in the HTDMA and the SMPS, and that of the CCNC were 10:1. The sample flow rates of DMA1 and DMA2 in the HTDMA were 0.65 and 0.3 L min^{-1}, respectively. The sample flow rates of CPC1, CPC2, and CCNC were 0.3, 0.3, and 0.05 L min^{-1}, respectively.

2.2. Calibration and Data Processing

The details of the calibration methods for the HTDMA, CCNC, and SMPS, and the data processing procedure were described in *Kawana et al.* [2016]. We provide a brief explanation of the calibration and data processing, and an explanation of the results from the calibration. The sizing performance of DMA1 in the HTDMA and the SMPS was examined using standard polystyrene spherical latex (PSL) particles with diameters of 48 ± 1, 100 ± 3, and 309 ± 9 nm (STADEX, JSR Corporation, Japan) before the observation. The mode diameters from a lognormal fitting to the measured size distributions for the 48, 100, and 309 nm PSL particles using DMA1 in the HTDMA were 50.7 ± 0.5, 99.0 ± 0.2, and 300.7 ± 0.7 (n = 3), respectively. Those using the DMA in the SMPS were 50.9 ± 0.4, 100.6 ± 0.1, and 304.0 ± 0.8 (n = 3), respectively. The hygroscopic growth factor (g) is defined as the ratio of the electrical mobility diameter under a humidified conditions ($d_{p,wet}$, 85% RH) to that under dry conditions ($d_{p,dry}$, RH < 2%) using the HTDMA. The size-resolved g distributions of ammonium sulfate (purity: 99.999%, Sigma-Aldrich) were obtained at the $d_{p,dry}$ of 24.1–359 nm with corrections for the difference in the sizing of DMA1 and DMA2 (<3%) and the width of the transfer functions of the DMAs [*Mochida et al.,* 2010; *Kawana et al.,* 2016]. The mode g values from a lognormal fitting to the g distributions agreed within 2% with those from the literature [*Tang and Munkelwitz*, 1994]. For atmospheric particles, the hygroscopic growth factor distributions n ($\log d_{p,dry}$, $\log g$), whose integral along the $\log g$ axis equals $dN_{CN}/d\log d_{p,dry}$, were obtained for the specific $d_{p,dry}$ from 24.1 to 359 nm (different sets of 34 diameters for respective supersaturation (SS) values) and for $0.8 \le g \le 2.2$. The n ($\log d_{p,dry}$, $\log g$) data for every 3 h were obtained (n = 80). The mean g for the g distributions at the respective $d_{p,dry}$, g_m and average g that corresponded to the mean volume of water retained by particles, g_{mw}, were calculated by the following equations:

$$g_m = \frac{\sum n(\log d_{p,\,dry},\ \log g) \bullet g}{\sum n(\log d_{p,\,dry},\ \log g)} \quad (0.8 \le g \le 2.2) \tag{1}$$

$$g_{mw} = \left[\left(\frac{\sum n(\log d_{p,\,dry},\ \log g) \bullet (g^3 - 1)}{\sum n(\log d_{p,\,dry},\ \log g)} \right) + 1 \right]^{\frac{1}{3}} \quad (0.8 \le g \le 2.2) \tag{2}$$

Here the range of 0.8–2.2 for g was selected to calculate g_m and g_{mw} regardless of the presence/absence of particles. The broadening of the g distributions from the shape of the DMA transfer functions was corrected [*Mochida et al.,* 2010]. The presence of particles with $g < 1$ after the correction (see section 4) suggests that broadening remained to some extent as expected from the data processing. The bias of the g distributions from the evaporation of volatile materials in the HTDMA was not assessed in this study. The CCN efficiency spectra, which are functions of the number-based ratios of CCN to CN versus $d_{p,dry}$ (24.1–359 nm), were obtained with corrections for the presence of multiply-charged particles under the consideration of the diffusion losses of particles in the tubing and the width of the transfer functions of the DMAs [*Mochida et al.,* 2010; *Kawana et al.,* 2016]. The fitting parameters for the CCN efficiency spectra, F_{act}, d_{act}, and σ in equation (3) [*Rose et al.,* 2008], were obtained with the method in *Kawana et al.* [2016].

$$f_{fit} = \frac{F_{act}}{2}\left[1 + \mathrm{erf}\left(\frac{d_{p,\,dry} - d_{act}}{\sigma\sqrt{2}}\right)\right] \tag{3}$$

The CCN efficiency spectra of ammonium sulfate particles were obtained to examine the supersaturation (SS) conditions in the CCNC. The SS values were determined to be 0.12%, 0.23%, and 0.41% from the d_{act} values of ammonium sulfate particles. The N_{CN} values of atmospheric aerosols in this study were from the SMPS data in the range of $24.1 \le d_{p,dry} \le 359$ nm. The N_{CCN} values of atmospheric aerosols were calculated from the SMPS-derived aerosol number-size distributions and the size-resolved CCN/CN ratios (measured values with the above mentioned multiply-charged particle correction), both of which were in the range of $24.1 \le d_{p,dry} \le 359$ nm, with interpolation.

The screenings of the SMPS, HTDMA, and CCNC data for the above analyses were performed as follows. To reduce possible influences from local anthropogenic activities such as the use of vehicles and cooking, if the 10 min average of the SMPS-derived number concentrations showed a ≥30% increase and the next 10 min average showed a ≥30% decrease, the SMPS and HTDMA data during the 10 min with the ≥30% increase and the 5 min data both just before and just after these 10 min were omitted. The omitted fraction of these data from the screening was 6%. The SMPS data after the screening were used to calculate N_{CN} and derive the absolute values of the size-resolved g distributions. The CCN data collected under inappropriate conditions of the CCNC were not used. Furthermore, the CCN efficiency spectra during 0300–0600 JST on 21 August and 1500–1800 JST on 22 August were discarded because the fraction of the omitted CCN data were large (>10%). The SMPS, HTDMA, and CCNC data during 0900–1200 JST on 27 August were also omitted because of the maintenance of the measurement system.

2.3. Derivation of the Hygroscopicity Parameter κ

Particle growth by the absorption of water vapor is explained by the Köhler equation, which describes the water vapor saturation ratio (S) at the air-particle interface versus the droplet diameter. The Köhler equation with a single hygroscopicity parameter κ (κ-Köhler equation [*Petters and Kreidenweis,* 2007]) represents the relationship as follows:

$$S = \frac{{d_{p,\,wet}}^3 - {d_{p,\,dry}}^3}{{d_{p,\,wet}}^3 - {d_{p,\,dry}}^3(1-\kappa)}\exp\left(\frac{4\sigma_s M_w}{RT\,\rho_w\,d_{p,\,wet}}\right) \tag{4}$$

where σ_s is the surface tension, M_w is the molecular weight of water, R is the universal gas constant, T is the absolute temperature, and ρ_w is the density of water. In this study, the κ values were obtained under subsaturated and supersaturated conditions. The κ values of particles under subsaturated water vapor conditions (~85% RH), κ_{HTDMA}, were calculated from the size-resolved g by the following equation:

$$\kappa_{HTDMA} = \left(g^3 - 1\right)\left[\frac{\exp\left(\frac{4\sigma_s M_w}{RT\,\rho_w\,d_{p,\,wet}}\right)}{0.85} - 1\right] \tag{5}$$

Similarly, representative κ values for specific mobility dry diameters were calculated by inputting g_{mw} as g in equation (5), which are referred to as $\kappa_{HTDMA,mw}$. The κ values under supersaturated water vapor conditions, κ_{CCNC}, were obtained by searching the values so that the maximum of S corresponds to the SS conditions in the CCNC (0.12%, 0.23%, and 0.41%) with the measured CCN activation diameters. When calculating κ_{HTDMA},

$\kappa_{HTDMA,mw}$, and κ_{CCNC}, T were assumed to be 298 K (the mean temperature of the sheath air that exited DMA2 in the HTDMA) and 300 K (the mean temperature of the top of the CCNC column). The σ_s values were assumed to be that of pure water in both calculations and were calculated by considering the temperature dependence [*Hänel,* 1976].

2.4. Cloud Parcel Model

To investigate the effects of hygroscopicity and particle size on cloud droplet activation, two different analyses were performed using a cloud parcel model with inputs from the size-resolved g distributions ($24.1 \leq d_{p,dry} \leq 359$ nm), which were measured every 3 h. One was a sensitivity analysis to assess the effect of g distributions with different hygroscopicity on N_{CD} [*Kawana et al.,* 2014]. Moreover, the relative contributions from particles with different hygroscopicity in the size ranges of the Aitken ($d_{p,dry} \leq 100$ nm) and accumulation ($100 \leq d_{p,dry} \leq 359$ nm) modes to the N_{CD} were investigated. The preparation of the inputs from the size-resolved g distributions and calculations of N_{CD} was described in *Kawana et al.* [2014]. All particles smaller than 359 nm were converted to those with the same critical SSs but with κ values of pure ammonium sulfate (0.61) by the adjustment of diameters, and particles larger than 359 nm, whose size distributions were measured (<735 nm) or extrapolated (>735 nm), were assumed to have κ values of pure ammonium sulfate without the diameter adjustment. The model used was similar to that in the work by *Kawana et al.* [2014] but modified to assess the contributions from particles with different ranges of diameter and g. The air parcel rose 150 m from the cloud base (970 hPa) adiabatically with updraft velocities (v) of 0.1, 0.5, 1.0, and 5.0 m s^{-1}, and the mean (range) maxima of the SS from individual runs ($n = 80$) under these conditions were 0.17% (0.12%–0.23%), 0.39% (0.30%–0.50%), 0.57% (0.44%–0.72%), and 1.3% (1.1%–1.7%), respectively. For the sensitivity analysis, the cloud droplet activation of particles was calculated by including all particles with a hygroscopicity of $0.8 \leq g \leq 2.2$ (base case) and particles in the ranges of $1.3 \leq g \leq 2.2$ and $1.45 \leq g \leq 2.2$.

Moreover, to assess the relative contributions from particles with different sizes and hygroscopicity to cloud droplet formation, the contributions from the following four groups were considered: less hygroscopic particles in the Aitken-mode range ($0.8 \leq g < 1.3$), less hygroscopic particles in the accumulation-mode range ($0.8 \leq g < 1.45$), more hygroscopic particles in the Aitken-mode range ($1.3 \leq g \leq 2.2$), and more hygroscopic particles in the accumulation-mode range ($1.45 \leq g \leq 2.2$). These ranges were based on the results for the mean g (g_m) values in the Aitken- and accumulation-mode ranges, which reached ~1.3 and ~1.45 on NPF event days (section 4.2). All aerosol particles larger than 359 nm were assigned to more hygroscopic particles in the accumulation-mode range. The N_{CCN} at the maximum supersaturation conditions in each model run was also calculated by counting the particles that had lower critical supersaturation (s_c) than the calculated maximum supersaturation. The contribution of N_{CCN} of particles with different hygroscopicity and sizes was assessed as with N_{CD}.

In the cloud parcel model, droplets whose radii were ≥1 μm were regarded as cloud droplets. The N_{CD} at an altitude of 100 m above the cloud base was used for the analysis in this study. Regardless of model runs, this height was higher than the heights with maximum supersaturation. The changes in N_{CD} with height at ~100 m above the cloud base were already small (from −0.24% to −0.02% m^{-1}).

3. Overview of the Studied Aerosols

The aerosol number-size distributions from the SMPS and the mass concentrations of aerosol components from a high-resolution time-of-flight aerosol mass spectrometer (HR-ToF-AMS) and offline chemical analysis during this observation have been reported elsewhere [*Han et al.,* 2013, 2014]. Backward air mass trajectories showed that the air masses originated from the Asian continent and urban areas in Japan on the first 6 days (from 0600 JST, 20 August to 0600 JST, 26 August). Aerosols at the observation site were abundant with ammonium sulfate and low-volatility OOA (LV-OOA) under the influence of the inflow of aged aerosols. The number-size distributions had relatively large mode diameters (around 100 nm) compared with those during the last 4 days (from 0600 JST, 26 August to 0600 JST, 30 August). The air mass trajectories showed that clean maritime air masses that originated from the Pacific Ocean arrived at the observation site during the last four days. Bursts of small particles (dry mobility diameter $d_{p,dry}$: ~30 nm) in the daytime and their subsequent rapid growth were observed, indicating the formation of new particles and their growth. In the

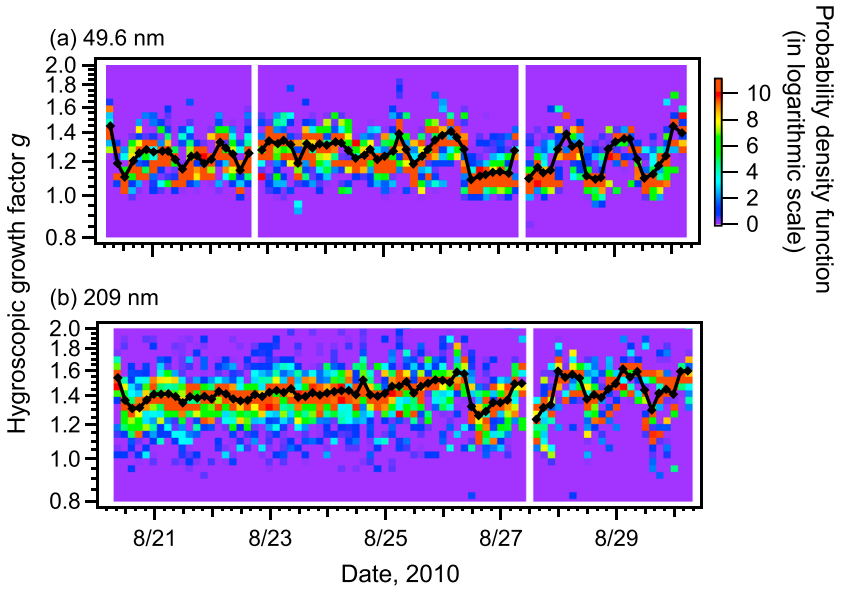

Figure 1. Time series of the g distributions at 85% RH for particles with $d_{p,dry}$ of (a) 49.6 nm and (b) 209 nm. The symbols represent the mean values of g (g_m) in the range of $0.8 \leq g \leq 2.2$.

daytime, the fraction of semivolatile oxygenated organic aerosol (SV-OOA, with an oxygen to carbon atomic ratio of 0) increased, suggesting the local photochemical formation of BSOA. The oxidation state as an index of the O/C ratio of organics and f_{44} (the ratio of the signal intensity at m/z 44, typically from COO^+, to the total signal intensity from OA) increased from the afternoon to nighttime, suggesting the aging of the aerosols.

4. Results and Discussion

4.1. Time Series of Hygroscopic Growth Factors

The time series of the hygroscopic growth factor g of aerosol particles at 49.6 nm (in the Aitken-mode range) and 209 nm (in the accumulation-mode range), and the mean g (g_m) at these diameters is presented in Figure 1. The statistical values of g_m for the two diameters and some other diameters are summarized in Table 1. The g_m tended to be larger as the particle sizes increased. The temporal variations in the growth factor distributions at 49.6 and 209 nm (Figure 1) were similar. On NPF event days, strong diurnal variations were observed for both sizes. During the daytime, less hygroscopic particles ($g \sim 1.1$) were dominant and the g_m was low. In the evening and nighttime, more hygroscopic particles appeared and the g_m increased. This tendency appeared regardless of the particle size in general (Table 1). On the other hand, the diurnal variation patterns on nonevent days were not strong at either 49.6 or 209 nm, although the smaller particles showed weak temporal variations within a day. The diurnal variations in the g_m values on nonevent and NPF event days for five dry diameters are presented in Figure 2. On NPF event days, g_m decreased markedly around 1000 JST and increased in the evening toward midnight. Although similar variations were observed on nonevent days, the variation patterns were not very clear for large particles (209 and 300 nm). Two different time periods (0900–2100 and 2100–0900 JST) were subjected to analysis according to the variation pattern of g_m (low in daytime and high in nighttime) in later sections.

As shown in Figure 1, the hygroscopic growth of particles was characterized by unimodal g distributions. Unimodal distributions have been observed at some other forest sites [*Hong et al.,* 2014], whereas multimodal distributions have also been reported [*Hämeri et al.,* 2001; *Irwin et al.,* 2011]. A nearly hydrophobic mode, which is observed for urban aerosols [*McFiggans et al.,* 2006], was absent, indicating a small contribution from locally emitted anthropogenic primary particles, i.e., particles composed of hydrocarbon-like organic aerosol (HOA) and black carbon (BC). The changes in the unimodal g distributions were analyzed with respect to the size-resolved distributions, as presented below.

Table 1. Hygroscopic Growth Factors and Hygroscopicity Parameters of Aerosol Particles[a]

Period	$d_{p,dry}$ (nm)	g_m	$\kappa_{HTDMA,mw}$
0900–2100 JST, nonevent days	28.9	1.23 ± 0.12	0.22 ± 0.15
	49.6	1.23 ± 0.05	0.20 ± 0.05
	102	1.29 ± 0.06	0.23 ± 0.06
	209	1.40 ± 0.05	0.33 ± 0.06
	359	1.47 ± 0.06	0.40 ± 0.07
	mean[b]	1.30 ± 0.10	0.26 ± 0.07
	Ait[c]	1.23 ± 0.04	0.20 ± 0.02
	Acc[d]	1.39 ± 0.06	0.33 ± 0.06
0900–2100 JST, NPF event days	28.9	1.12 ± 0.06	0.11 ± 0.07
	49.6	1.14 ± 0.07	0.12 ± 0.07
	102	1.21 ± 0.07	0.16 ± 0.06
	209	1.35 ± 0.07	0.28 ± 0.07
	359	1.36 ± 0.19	0.30 ± 0.19
	mean[b]	1.23 ± 0.10	0.19 ± 0.08
	Ait[c]	1.15 ± 0.04	0.12 ± 0.02
	Acc[d]	1.34 ± 0.05	0.27 ± 0.05
2100–0900 JST, nonevent days	28.9	1.27 ± 0.10	0.28 ± 0.13
	49.6	1.30 ± 0.06	0.27 ± 0.07
	102	1.34 ± 0.07	0.29 ± 0.08
	209	1.44 ± 0.05	0.38 ± 0.06
	359	1.47 ± 0.08	0.40 ± 0.08
	mean[b]	1.36 ± 0.07	0.32 ± 0.05
	Ait[c]	1.30 ± 0.03	0.28 ± 0.01
	Acc[d]	1.43 ± 0.04	0.37 ± 0.04
2100–0900 JST, NPF event days	28.9	1.22 ± 0.11	0.23 ± 0.02
	49.6	1.28 ± 0.10	0.26 ± 0.05
	102	1.40 ± 0.09	0.35 ± 0.06
	209	1.52 ± 0.08	0.47 ± 0.06
	359	1.52 ± 0.18	0.49 ± 0.07
	mean[b]	1.38 ± 0.12	0.35 ± 0.11
	Ait[c]	1.29 ± 0.06	0.27 ± 0.05
	Acc[d]	1.50 ± 0.04	0.46 ± 0.05
All periods	28.9	1.22 ± 0.11	0.22 ± 0.03
	49.6	1.25 ± 0.09	0.22 ± 0.01
	102	1.32 ± 0.09	0.26 ± 0.02
	209	1.43 ± 0.08	0.36 ± 0.06
	359	1.46 ± 0.12	0.40 ± 0.02
	mean[b]	1.33 ± 0.10	0.29 ± 0.07
	Ait[c]	1.25 ± 0.04	0.23 ± 0.01
	Acc[d]	1.42 ± 0.05	0.35 ± 0.05

[a]Mean ± SD.
[b]Mean ± SD of individual values for 16 diameters in the range of 24.1–359 nm (24.1, 28.9, 34.6, 41.4, 49.6, 59.4, 71, 85.1, 102, 122, 146, 175, 209, 250, 300, and 359 nm).
[c]Mean ± SD of individual values for 9 diameters in the range of 24.1–102 nm among the above 16 diameters.
[d]Mean ± SD of individual values for 7 diameters in the range of 122–359 nm among the above 16 diameters.

4.2. Two-Dimensional Hygroscopic Growth Factor Distributions

The hygroscopic growth factor distributions were analyzed for four different time sections according to the absence/presence of NPF events within a day and for different periods. These periods were determined from the characteristics of the size-resolved g_m values (Figure 2) and growth factor distributions (Figure 3). The averages of the size-resolved g distributions ($d_{p,dry}$: 24.1–359 nm, $0.8 \leq g \leq 2.2$) at 85% RH in four time sections are presented in Figure 3. The particle hygroscopicity tended to be low during 0900–2100 JST and high during 2100–0900 JST. Moreover, the size-resolved g distributions during 0900–2100 JST showed marked differences between nonevent and NPF event days. Each of the g distributions and those normalized distributions during 1200–1500 and 0000–0300 JST over 10 days are presented in the supporting information (Figures S1–S4), which also showed the same characteristics depending on nonevent/NPF event days and the time of day.

On NPF event days, the g distributions depended primarily on the time sections. Temporal variation was also evident from the averages of the logarithmetically spaced g probability density factions (log-spaced g-PDF) for every 3 h (Figure 4). During 0900–2100 JST, large number concentrations of less hygroscopic particles were observed in the Aitken-mode range (Figures 3c and 4a–4d). With these bursts of nanoparticles, the formation of BSOA must have led to the predominance of fresh, less oxidized, and less hygroscopic particles ($g \sim 1.1$). The observation site during this period was influenced by clean maritime air masses, in which the aerosol number and mass concentrations were presumably low, which might have enhanced the contributions from the newly formed BSOA to the particle hygroscopicity. The inflow of highly hygroscopic components in the background aerosols should not have been a major contributor in the small size range because the mass concentrations of organics increased in $d_{va} < 300$ nm (corresponding to $d_{p,dry} < 150$ nm) without a marked increase in sulfate [*Han et al.,* 2014]. The low g values of particles in the Aitken-mode range at 24.1–102 nm (g_{Ait}: 1.15) were similar to those of laboratory-generated BSOA ($g \sim 1.1$) [*Varutbangkul et al.,* 2006; *Lang-Yona et al.,* 2010], which

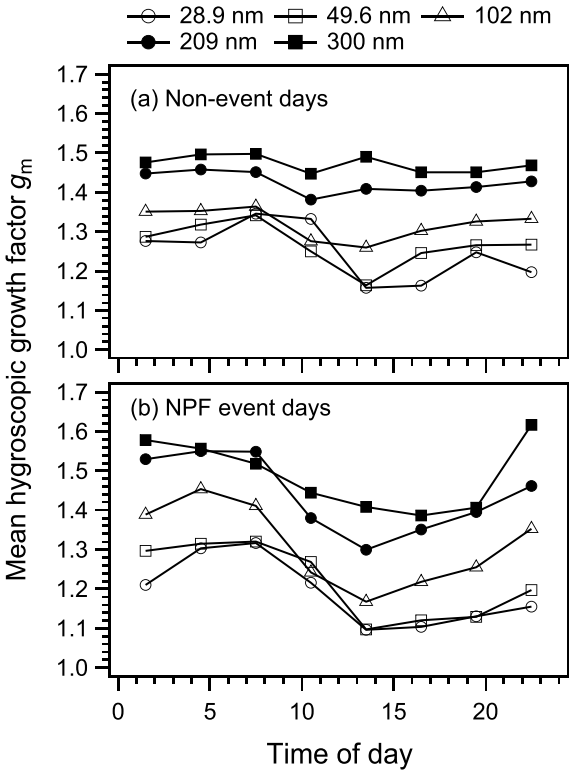

Figure 2. Diurnal variations of the mean g (g_m) at 85% RH for particles with $d_{p,dry}$ of 28.9, 49.6, 102, 209, and 300 nm during (a) nonevent days and (b) NPF event days. The symbols represent the mean values of g (g_m) in the range of $0.8 \leq g \leq 2.2$.

suggests that the particles were composed of newly formed BSOA from BVOCs. This result is supported by the results from chemical composition analysis using the AMS: the fraction of locally generated semivolatile oxygenated organic aerosol (SV-OOA) in organics was large [*Han et al.,* 2014]. The BSOA formation must have also influenced the particle hygroscopicity in the accumulation-mode range. The g of particles in the accumulation-mode range at 122–359 nm (g_{Acc}: 1.34) was lower than that on nonevent days, presumably because the condensation of less hygroscopic BSOA components decreased the g of preexisting particles.

During 2100–0900 JST on the NPF event days, the distributions of g shifted to the larger side (Figures 3d and 4e–4h) and the mean g (g_m) in both the Aitken- and accumulation-mode ranges were high (g_{Ait}: 1.29 and g_{Acc}: 1.50). Possible reasons include the aging (oxidation) of newly formed BSOA, the formation of water-soluble secondary organic aerosol (SOA) in the aqueous phase under elevated RH conditions, and the inflow of highly hygroscopic components in the background aerosols. The aging of BSOA was inferred from the increase in the O/C ratio of organics and f_{44} from the AMS analysis [*Han et al.,* 2014]. The nighttime formation of water-soluble organics under high RH conditions has been suggested for different environments, including a forest environment [*Hennigan et al.,* 2008, 2009; *Miyazaki et al.*, 2012]. Contributions from the inflow of highly hygroscopic components in the background aerosols could not be ruled out because the mass spectral analysis suggested the gradual replacement of BSOA with background aerosols [*Han et al.,* 2014]. At >200 nm, high g values up to 1.8 were observed in the nighttime (Figure 4). Sulfate, which likely originated from the Pacific, was mainly in a large diameter range ($d_{p,dry} > 150$ nm) during these periods and likely led to the increase in g.

On nonevent days (Figures 3a–3b and 5), broad unimodal g distributions with intermediate hygroscopic particles (range: 1.2–1.4) were observed. The differences in the g distributions in different time sections were not clear. The averages of the log-spaced g-PDF for every 3 h are presented in Figure 5, which also shows similar distributions throughout each day. The g_{Ait} and g_{Acc} values during 0900–2100 JST were 1.23 and 1.39, respectively, whereas those during 2100–0900 JST were 1.30 and 1.43, respectively (Table 1). The g_m values during 0900–2100 JST were slightly lower than those during 2100–0900 JST, which was likely caused by the local formation of BSOA with less hygroscopicity. More hygroscopic particles must have been dominant in the background air from the Asian continent and Japan throughout these days, which explains the small differences. The unimodal g distributions on nonevent days can be explained as follows. The observation site was influenced by air masses with long-range transport, and aged particles (ammonium sulfate and low-volatility OOA (LV-OOA)) were dominant [*Han et al.,* 2013, 2014]. Therefore, internally mixed, aged, and highly oxidized aerosols with a relatively more hygroscopic nature ($g \sim 1.2$–1.4) were abundant over these days and formed unimodal g distributions. *Mochida et al.* [2010] reported that the g distributions in Okinawa, a remote receptor site of the Asian outflow, were characterized mostly by unimodal distributions with highly hygroscopic particles (median g: 1.39–1.47 at 49–125 nm). In the

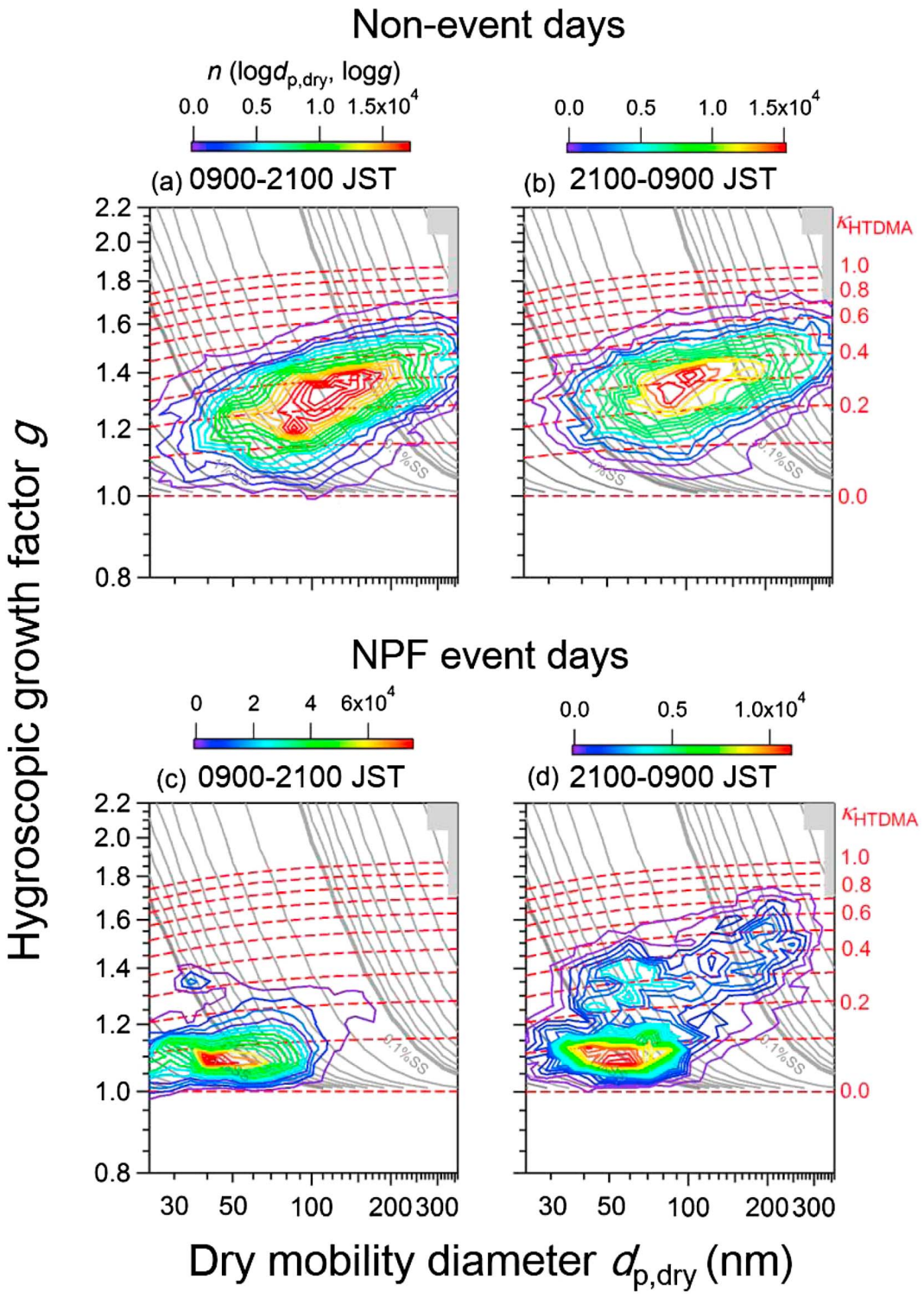

Figure 3. Average of the two-dimensional distributions of the number concentrations of aerosol particles as a function of the hygroscopic growth factor (g) and dry mobility diameter ($d_{p,dry}$) at 85% RH during (a) 0900–2100 and (b) 2100–0900 JST on nonevent days and during (c) 0900–2100 and (d) 2100–0900 JST on NPF event days. The dashed red lines represent the contours of κ_{HTDMA} at 85% RH. The gray contours show the critical SS estimated from the κ-Köhler theory [*Mochida et al.,* 2011].

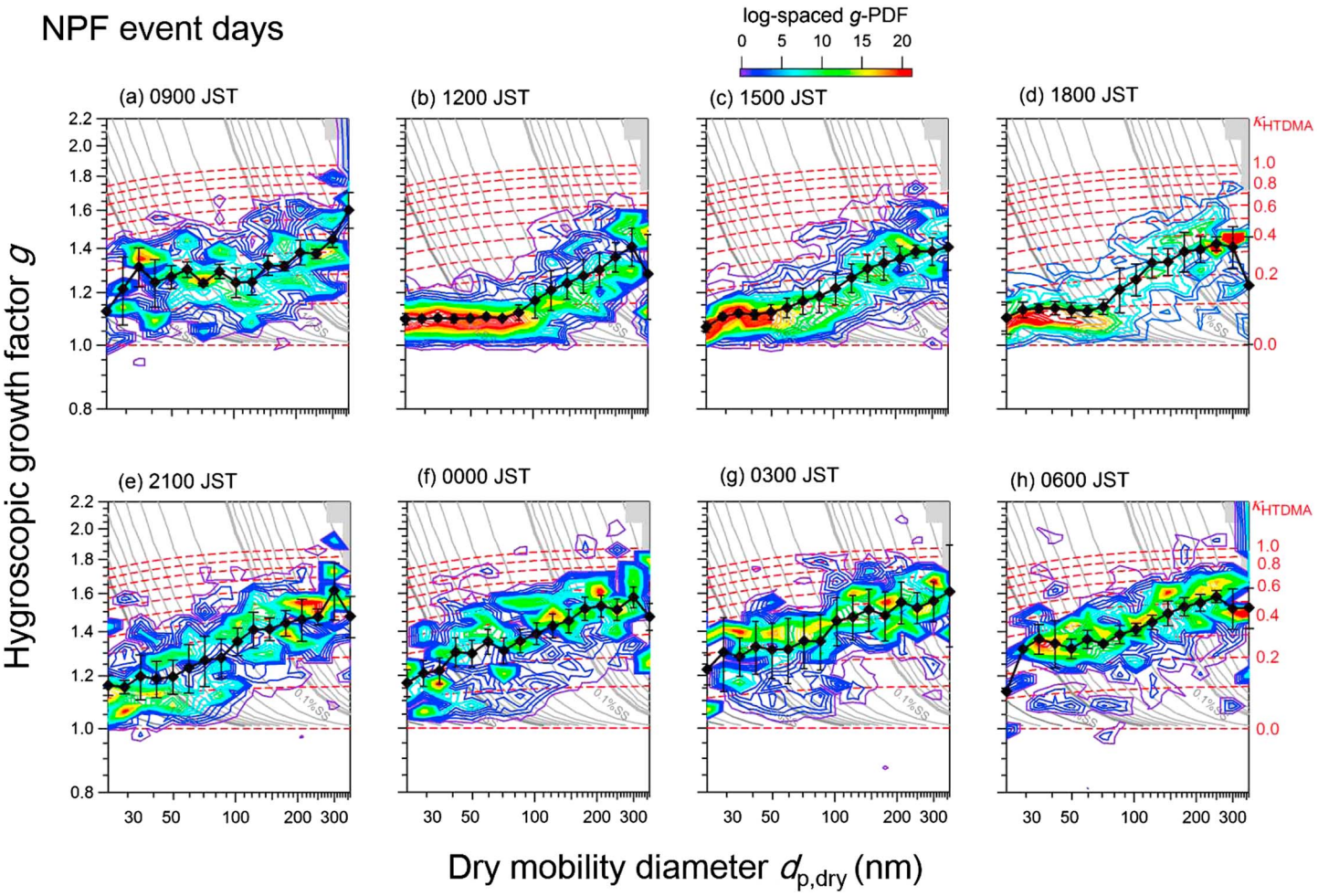

Figure 4. Averages of the logarithmically spaced g probability functions (log-spaced g-PDF) at 85% RH during (a) 0900–1200, (b) 1200–1500, (c) 1500–1800, (d) 1800–2100, (e) 2100–2400, (f) 0000–0300, (g) 0300–0600, and (h) 0600–0900 JST, on NPF event days. The solid symbols represent the mean values of g in the range of $0.8 \leq g \leq 2.2$ at 24.1–359 nm. The bars represent the standard deviations.

present study, the hygroscopicity lower than those in Okinawa were observed, which could be partially explained by the local addition of BSOA with less hygroscopicity.

The number-size distributions and the number fractions of particles in different ranges of g are summarized in Figure 6. During 0900–2100 JST on NPF event days (Figures 6e and 6f), large N_{CN} and a large fraction of less hygroscopic particles were observed, particularly in the Aitken-mode range. The fraction of more hygroscopic particles in this period was lower than those in the other time sections. Less hygroscopic particles were dominant (>50%) up to 180 nm. In other time sections, the averages of the number-size distributions and the number fractions were characterized by a large fraction of more hygroscopic particles ($g \geq 1.25$), which contrasts the results at an urban site [*Kawana et al.,* 2016] with large N_{CN} and a large fraction of less hygroscopic particles ($g < 1.25$). During 2100–0900 JST on NPF event days (Figures 6g and 6h), the lowest N_{CN} and largest fraction of more hygroscopic particles were observed among four different time sections. This characteristic was also observed even if data for 0600–0900 JST on 26 August were omitted, to precisely assess the characteristics after the period of 0900–2100 JST (Figure S5). The large fraction of more hygroscopic particles might have been caused by the chemical aging of newly formed BSOA and the production of water-soluble organics. At >200 nm, the inflow of maritime airs must have also increased the particle hygroscopicity, as explained above. During 0900–2100 JST on nonevent days (Figures 6a and 6b), intermediate hygroscopic particles ($1.1 \leq g < 1.4$) were dominant and the number concentrations of more hygroscopic particles ($g \geq 1.4$) in the large diameter range were high. During 2100–0900 JST (Figures 5c and 5d), the

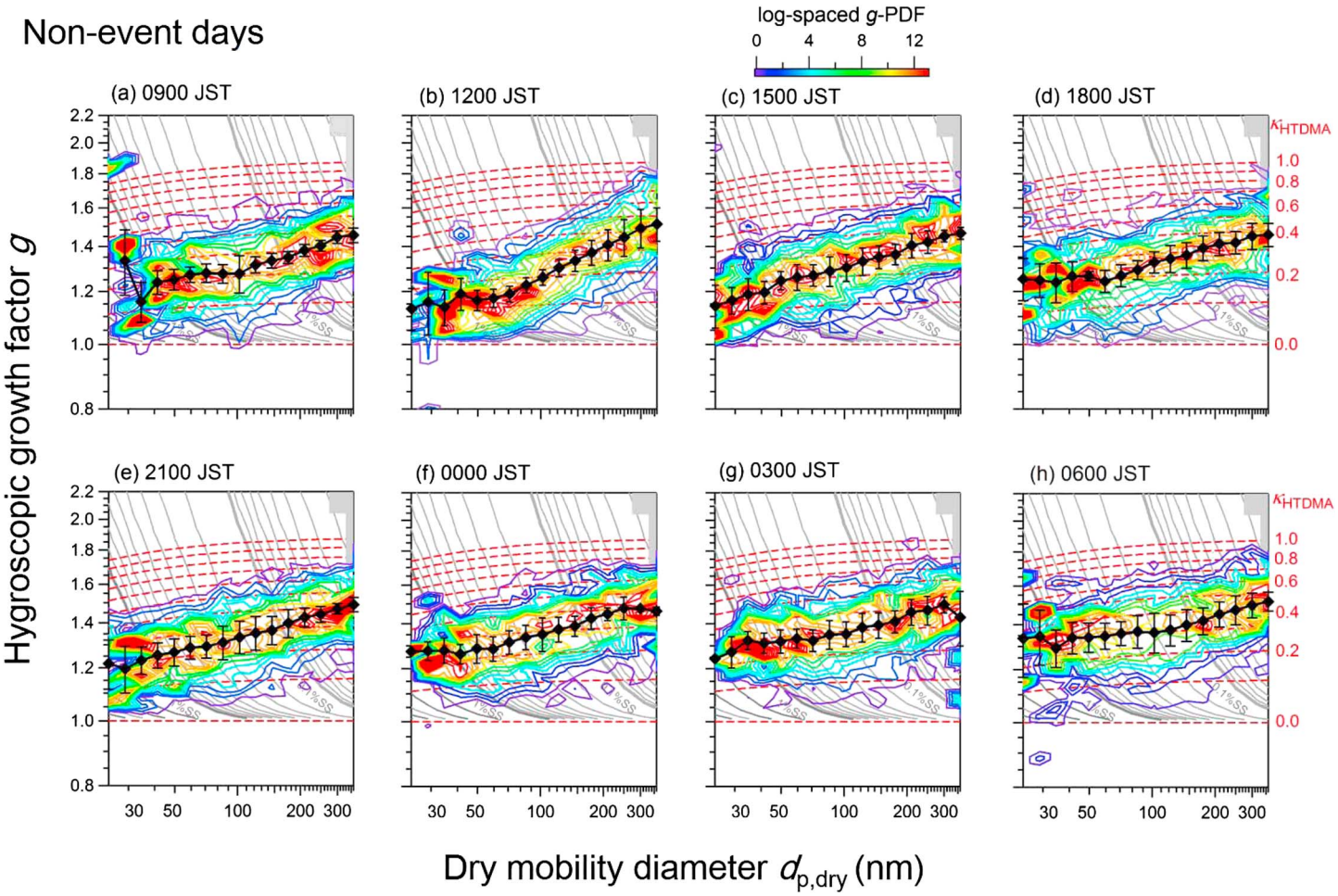

Figure 5. The same information as in Figure 4 but for nonevent days.

shapes of the average number-size distributions at the respective *g* ranges were not greatly different from those during 0900–2100 JST. However, the number concentration of less hygroscopic particles was on average half that during 0900–2100 JST, and the fraction of more hygroscopic particles was, in general, relatively large.

4.3. CCN Activity

The time series of the CCN-activated fraction (F_{act}) and the CCN activation diameter (d_{act}) at 0.12%, 0.23%, and 0.41% SS, both from the curve fitting to the CCN efficiency spectra in equation (3), are presented in Figures 7a–7c. The F_{act}, d_{act}, and CCN-activated fraction at a maximum diameter of 359 nm (F_{max}) are summarized in Table 2. The F_{act} and F_{max} were on average ≥0.85, which indicates that the fractions of CCN-inactive particles well above d_{act} were generally small. During 0900–2100 JST on NPF event days, the fractions of CCN-inactive particles were larger than those in other time sections regardless of the SS conditions, which suggest the predominance of less hygroscopic organic compounds. The diurnal variations of d_{act} on NPF event days were large under all SSs (0.12%–0.41% SS) compared with those on nonevent days; the d_{act} values during 0900–2100 JST were large and those during 2100–0900 JST were small (Figures 7a–7c). The averages of the CCN efficiency spectra and the fitted curves also suggest differences between NPF event and nonevent days and between 0900–2100 and 2100–0900 JST (Figures 8a–8c). These results match the differences in the *g* distributions for the four time sections. During 0900–2100 JST on NPF event days, small particles with low hygroscopicity, which should have had large critical supersaturation (s_{crit}) for activation, were dominant, in accordance with relatively large d_{act}. This result indicates the effect of BSOA on the CCN activity of the particles. During 2100–0900 JST, more hygroscopic large particles were dominant, in accordance with large F_{act} and relatively small d_{act}.

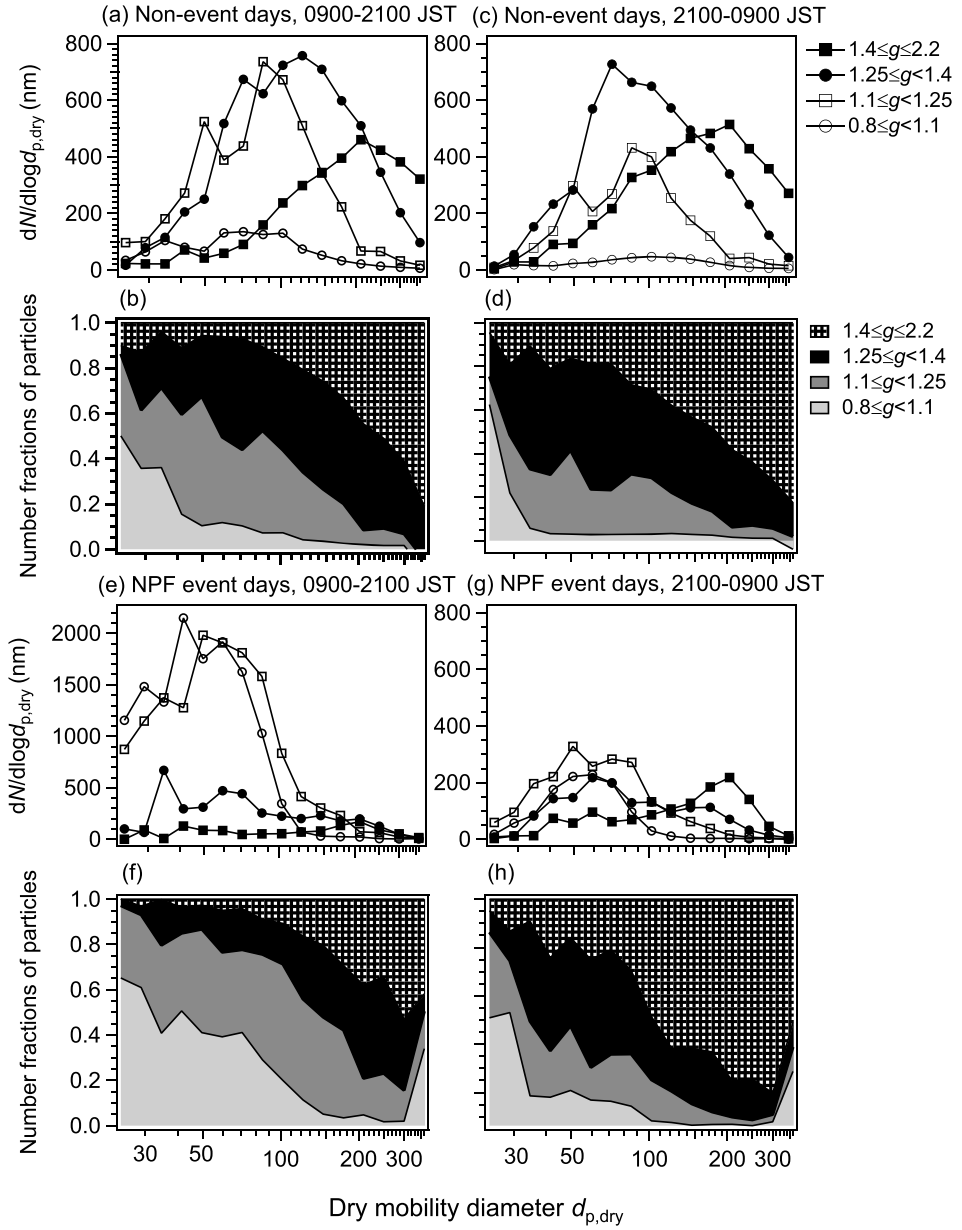

Figure 6. Averages of (a) the number-size distributions and (b) the number fractions of aerosol particles in the ranges of $0.8 \le g < 1.1$, $1.1 \le g < 1.25$, $1.25 \le g < 1.4$, and $1.4 \le g \le 2.2$ during 0900–2100 JST on nonevent days. (c and d) Same as Figures 6a and 6b but during 2100–0900 JST on nonevent days. (e and f) Same as Figures 6a and 6b but during 0900–2100 JST on NPF event days. (g and h) Same as Figures 6a and 6b but during 2100–0900 JST on NPF event days.

The time series of N_{CN}, N_{CCN}, and the ratio of N_{CCN}/N_{CN} under three SS conditions are presented in Figures 7d and 7e. On NPF event days, N_{CCN} and N_{CCN}/N_{CN} increased following the afternoon in response to the burst of N_{CN}, which suggests that newly formed particles contributed to the increase in N_{CCN}. The mean values of N_{CCN} during 0900–2100 JST were 63, 117, and 155 cm^{-3} at 0.12%, 0.23%, and 0.41% SS, respectively, and those during 2100–0900 JST increased substantially (95, 202, and 360 cm^{-3}, respectively). On nonevent days, the mean values of N_{CCN} at 0.12%, 0.23%, and 0.41% throughout a day were 297, 543, and 674 cm^{-3}, respectively. Although the particle bursts resulted in large N_{CN} in the daytime and more hygroscopic and large particles were dominant in the nighttime on NPF event days, the mean values of N_{CCN} on NPF event days were lower than those on nonevent days. The mean N_{CCN}/N_{CN} values for NPF event days (or nonevent days) were 0.13 (0.29), 0.25 (0.49), and 0.36 (0.60) at 0.12%, 0.23%, and 0.41% SS, respectively.

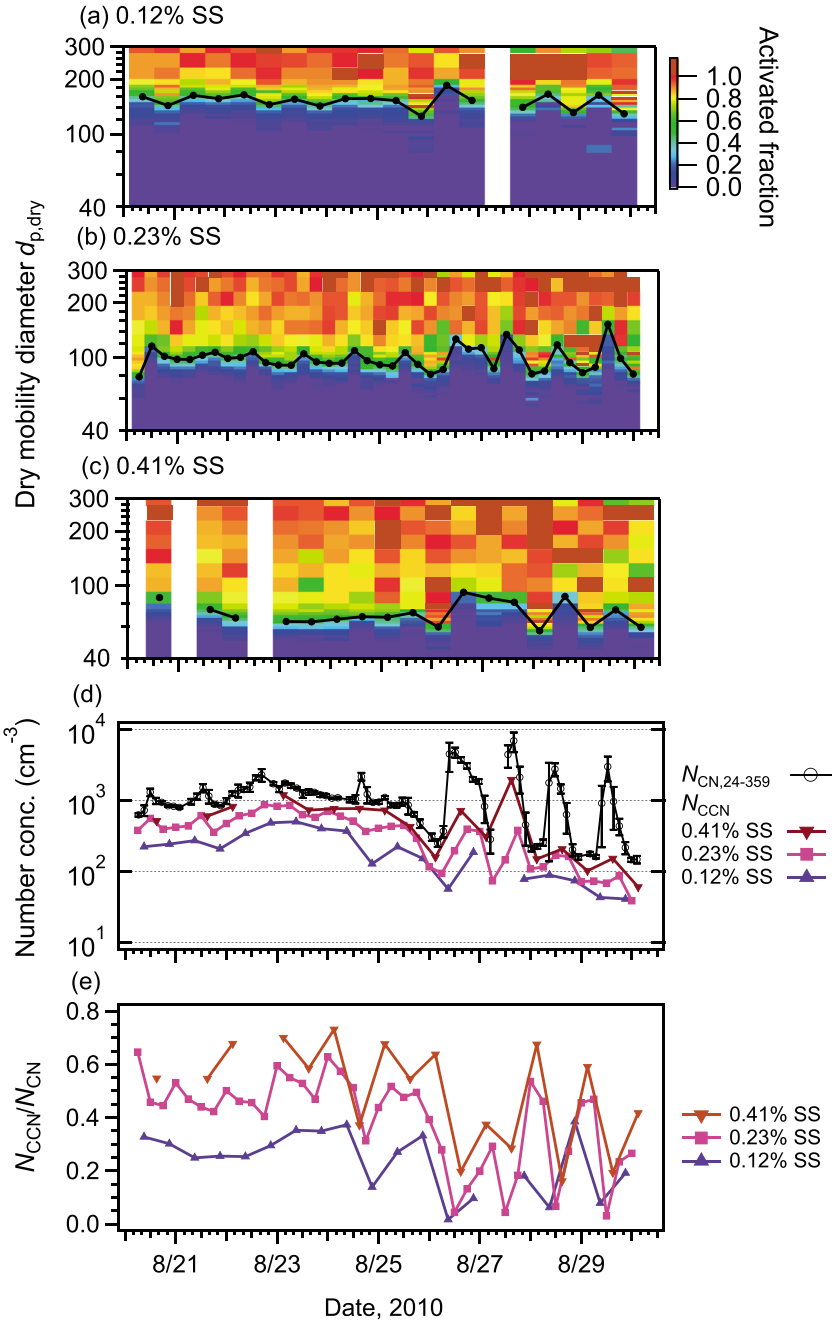

Figure 7. (a–c) Time series of the size-resolved CCN-activated fractions at $d_{p,dry}$ under 0.12%, 0.23%, and 0.41% SS. (d) Time series of the number concentrations of CCN (N_{CCN}) and CN (N_{CN}) in the size range of 24.1–359 nm. The bars in the N_{CN} represent the standard deviations. (e) Time series of the ratios of N_{CCN} to N_{CN} under 0.12%, 0.23%, and 0.41% SS. The filled circles with solid lines in Figures 7a–7c represent the CCN activation diameters (d_{act}).

Compared with the previous studies, the mean N_{CCN} values during the observation in this study were similar to those over a tropical rainforest in Malaysia (61–274 cm^{-3} at 0.11%–0.37% SS [*Irwin et al.,* 2011]) and a forest in California (<500 cm^{-3} at 0.14%–0.36% SS [*Levin et al.,* 2012]) and higher than the mean N_{CCN} value in a pristine rainforest in Amazonia (35–160 cm^{-3} at 0.1%–0.8% SS [*Gunthe et al.,* 2009]). Figure 9 compares the mean values of N_{CCN}/N_{CN} for NPF event days and all periods from this study with those in the literature. For all the periods, the mean values of N_{CCN}/N_{CN} at around 0.4% SS were not very different from those of other forest sites [*Vestin et al.,* 2007; *Gunthe et al.,* 2009; *Sihto et al.,* 2011; *Levin et al.,* 2012] or from both

Table 2. Parameters of CCN Activation and Hygroscopicity Parameters for Aerosol Particles[a]

Period	SS	F_{act}	F_{max}	d_{act}	κ_{CCNC}
0900–2100 JST, nonevent days	0.41	0.89 ± 0.06	1.04 ± 0.22	73 ± 9	0.22 ± 0.02
	0.23	0.90 ± 0.04	0.96 ± 0.11	103 ± 7	0.24 ± 0.05
	0.12	0.92 ± 0.03	0.94 ± 0.11	159 ± 4	0.22 ± 0.02
	Mean[b]				0.23 ± 0.05
2100–0900 JST, nonevent days	0.41	0.93 ± 0.06	1.11 ± 0.30	65 ± 9	0.29 ± 0.08
	0.23	0.91 ± 0.04	0.94 ± 0.06	92 ± 7	0.33 ± 0.08
	0.12	0.93 ± 0.05	0.99 ± 0.10	145 ± 12	0.34 ± 0.12
	Mean[b]				0.31 ± 0.08
0900–2100 JST, NPF event days	0.41	0.88 ± 0.05	0.86 ± 0.17	84 ± 8	0.17 ± 0.03
	0.23	0.96 ± 0.07	0.97 ± 0.20	118 ± 19	0.17 ± 0.08
	0.12	0.89 ± 0.07	0.85 ± 0.14	171 ± 12	0.14 ± 0.04
	Mean[b]				0.16 ± 0.06
2100–0900 JST, NPF event days	0.41	0.93 ± 0.07	1.01 ± 0.17	65 ± 14	0.33 ± 0.07
	0.23	0.95 ± 0.07	0.94 ± 0.08	89 ± 10	0.39 ± 0.10
	0.12	0.92 ± 0.07	1.20 ± 0.50	138 ± 11	0.33 ± 0.14
	Mean[b]				0.36 ± 0.10
All periods	0.41	0.91 ± 0.06	1.02 ± 0.24	71 ± 11	0.26 ± 0.08
	0.23	0.91 ± 0.06	0.95 ± 0.12	100 ± 15	0.28 ± 0.10
	0.12	0.92 ± 0.03	1.00 ± 0.25	152 ± 15	0.25 ± 0.10
	Mean[b]				0.27 ± 0.10

[a]Mean ± SD.
[b]Calculated from individual values measured at all three supersaturations.

clean and polluted environments [*Andreae*, 2009]. The mean N_{CCN}/N_{CN} during 0900–2100 JST on NPF event days from this study was characterized by low values compared to those from other studies, as presented in Figure 9.

4.4. Hygroscopicity Parameter κ of Forest Aerosols and Organics

The hygroscopicity parameter κ, which was calculated from the *g* distributions ($\kappa_{HTDMA,mw}$) and the CCN activation diameters (κ_{CCNC}), is summarized in Tables 1 and 2, respectively. The $\kappa_{HTDMA,mw}$ and κ_{CCNC} were characterized by differences between NPF event and nonevent days, time sections, and differences in particle size. On NPF event days, the mean of $\kappa_{HTDMA,mw}$ for the Aitken- and accumulation-mode ranges and the mean of κ_{CCNC} for the respective SSs showed clear diurnal variations: the values during 0900–2100 JST were 41%–58% lower than those during 2100–0900 JST. The values during 0900–2100 and 2100–0900 JST on NPF event days were, respectively, 18%–40% lower and 0%–24% higher than those during respective periods on nonevent days.

The κ values of organics (κ_{org}) for newly formed particles during the daytime on NPF event days in the Aitken-mode range was estimated by assuming that the contributions from other components (EC, chloride, and ammoniated sulfate and nitrate) to the total particle hygroscopicity ($\kappa_{HTDMA,mw}$ or κ_{CCNC}) were negligible under the Zdanovskii-Stokes-Robinson (ZSR) mixing rule [*Petters and Kreidenweis,* 2007]. This assumption was based on the chemical composition observed using the AMS and filter analysis. During the daytime on NPF event days, the mass concentrations of organics in the Aitken-mode range (vacuum aerodynamic diameter of 60–150 nm, which corresponds to around 43–106 nm in volume equivalent diameter) increased substantially, whereas those of sulfate did not markedly increase [*Han et al.,* 2014]. The mean of $\kappa_{HTDMA,mw}$ in the Aitken-mode range and the mean of κ_{CCNC} at three SSs during 0900–2100 JST on NPF event days were 0.12 ± 0.02 and 0.16 ± 0.06, respectively, which are regarded as the estimates of κ_{org} at 85% RH and under supersaturated conditions, respectively. The corresponding values of $\kappa_{HTDMA,mw}$ and κ_{CCNC} during 2100–0900 JST on the event days were higher (0.27 ± 0.05 and 0.36 ± 0.10, respectively), which may have been influenced by the aging of BSOA [*Engelhart et al.,* 2008, 2011].

The κ values during 0900–2100 JST on NPF event days in the Aitken-mode range ($\kappa_{HTDMA,mw}$: 0.12, κ_{CCNC}: 0.16, κ_{org}: 0.12–0.16) from this study were similar to those of forest aerosols in previous studies and laboratory-generated BSOA (Table 3). The reported κ values of atmospheric forest aerosols, characterized

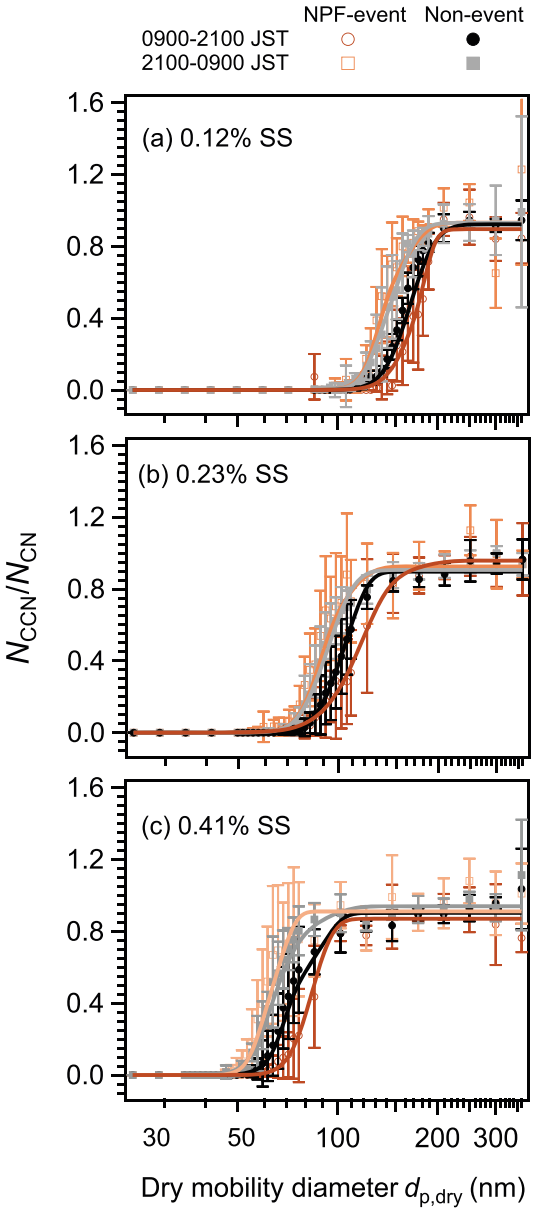

Figure 8. Averages of the measured CCN efficiency spectra and the fitted curves during 0900–2100 JST (circles) and 2100–0900 JST (squares) on NPF event (open markers) and nonevent days (filled markers) under (a) 0.12%, (b) 0.23%, and (c) 0.41% SS. The color of each fitted curve is the same as that of the corresponding average of the measured spectrum. The bars represent the standard deviation.

by the predominance of BSOA from HTDMA and CCNC, were slightly hygroscopic and ranged from 0.1 to 0.2: ~0.15 in the tropical rainforest in Amazonia [*Gunthe et al.,* 2009], ~0.13 and ~0.18 in boreal forests [*Cerully et al.,* 2011; *Sihto et al.,* 2011], and ~0.1 and ~0.13 in other forested sites [*Dusek et al.,* 2010; *Levin et al.,* 2014]. Laboratory-generated BSOA had κ values of 0.1–0.2 (0.15 from monoterpene and 0.12 from isoprene at 85% RH [*Engelhart et al.,* 2008, 2011]) and g values of 1.0–1.1 (1.06–1.10 from monoterpene and 1.01–1.04 from sesquiterpene at 85% RH [*Varutbangkul et al.,* 2006]).

The κ values under subsaturated and supersaturated conditions, $\kappa_{HTDMA,mw}$ and κ_{CCNC} values, were similar, as presented in Figure 10. For this figure, similar ranges of $d_{p,dry}$ were applied (diameter ranges for $\kappa_{HTDMA,mw}$ and mean ± SD of d_{act} for κ_{CCNC}: 136–169 nm and 152 ± 15 nm, 88–109 nm and 100 ± 15 nm, and 64–85 nm and 71 ± 11 nm, for κ_{CCNC} at 0.12%, 0.23%, and 0.41% SS, respectively), and the mean values of $\kappa_{HTDMA,mw}$ at seven diameters were used. The average of the ratios of κ_{CCNC} to $\kappa_{HTDMA,mw}$ was 0.99 ± 0.15, which means that the difference between κ_{CCNC} and $\kappa_{HTDMA,mw}$ was −1% ± 15% at three SS (n = 80). The difference in the $\kappa_{HTDMA,mw}$ values based on the measurement of ammonium sulfate particles from the values from the Köhler model, which incorporated the Pitzer equation [*Pitzer and Mayorga,* 1973], ranged from −7% to +7% for 16 sizes, so the observed −1% difference was not significant. On the other hand, the relative standard deviations (RSD) of $\kappa_{HTDMA,mw}$ and κ_{CCNC} for ammonium sulfate were 3% and 4%, respectively, the combination of which was smaller than 15%. However, this difference may not be insignificant either because the HTDMA and CCNC measurements of atmospheric particles may be influenced by changes in aerosol properties during data acquisition. In some studies, large differences (>30%) in HTDMA- and CCNC-derived κ values were observed in laboratory and ambient aerosol studies, which was related to the effects of organic compounds: the presence of sparingly soluble materials [*Wex et al.,* 2009], surface tension reduction [*Facchini et al.,* 1999, 2000; *Kiss et al.,* 2005; *Wex et al.,* 2008; *Good et al.,* 2010], the evaporation and/or co-condensation of semivolatile compounds [*Kristensen et al.,* 2012; *Topping and McFiggans*, 2012; *Wu et al.,* 2013], and the dependence

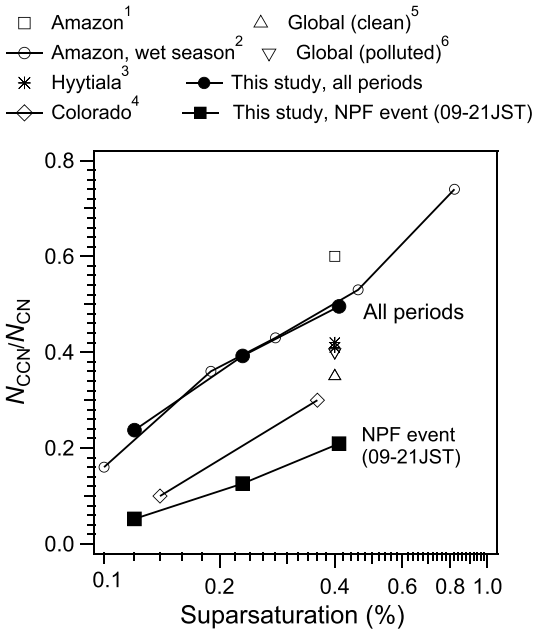

Figure 9. N_{CCN}/N_{CN} ratio as a function of SS in this study and those in forest environments (1: Amazon [*Vestin et al.,* 2007]; 2: Amazon during the wet season [*Gunthe et al.,* 2009]; 3: Hyytiälä [*Sihto et al.,* 2011]; 4: Colorado [*Levin et al.,* 2012]) and global environments (5: clean; 6: polluted) [*Andreae,* 2009].

of the activity coefficient of water on the concentration of the solution [*Prenni et al.,* 2007; *Wex et al.,* 2009; *Good et al.,* 2010; *Massoli et al.,* 2010]. For example, κ_{HTDMA} and κ_{CCNC} were different for urban aerosols (~37%), which suggests a large contribution from organics, as mentioned above [*Kawana et al.,* 2016]. The similarity between κ_{HTDMA} and κ_{CCNC} in this study suggests that the contribution from organics that may have caused these differences was small. Some studies have indicated that the contribution from surface tension reduction of BSOA was not large: the decrease in the surface tension was ~10 Nm^{-1}, or the surface tension could be assumed to be the same as that of pure water for CCN activation [*Engelhart et al.,* 2008, 2011]. The small contribution from BSOA to the surface tension might explain the small difference between κ_{HTDMA} and κ_{CCNC} in this study.

4.5. CCN Closure

The N_{CCN}/N_{CN} values were predicted based on the *g* of particles at 85% RH and compared with the measured N_{CCN}/N_{CN} to investigate the effects of the variations in *g* with different time sections, particle sizes, and *g* distributions on the CCN number concentrations in the studied forest environment. This closure study was performed with the inputs of (a) an averaged single *g* during the entire observation, (b) time-resolved bulk

Table 3. Summary of the κ Values of Forest Aerosol Particles

κ_{HTDMA}	κ_{CCNC}	κ_{org}	References
–	0.12–0.20 (mean) (0.10%–0.82% SS, 55–201 nm)	0.09–0.11 (from CCNC)	*Gunthe et al.* [2009]
–	0.22–0.44 (0.33%–0.74% SS, <100 nm)	~0.1 (from CCNC)	*Dusek et al.* [2010], NPF event
0.14–0.15 (mean) (90% RH, 30–50 nm)	0.19–0.22 (mean) (0.1%–1.8% SS, 40–80 nm)	0.12–0.14 (from HTDMA and CCNC)	*Cerully et al.* [2011]
0.17–0.37 (range) (90% RH, 32–258 nm)	0.05–0.37 (range) (0.11%–0.73% SS, 45–300 nm)	–	*Irwin et al.* [2011]
0.18 (mean) (90% RH, 35–110 nm)	–	–	*Sihto et al.* [2011]
–	0.15–0.22 (mean) (0.14%–0.97% SS, 40–180 nm)	0.13 (from CCNC)	*Levin et al.* [2014]
0.12 ± 0.02 (mean) 0.03–0.37 (range) (85% RH, 24–102 nm)	0.16 ± 0.06 (mean) 0.07–0.30 (range) (0.12%–0.41% SS, 60–152 nm)	0.12–0.16 (from HTDMA and CCNC)	This study, 0900–2100 JST, NPF event days
0.29 ± 0.07 (mean) 0.03–0.81 (range) (85% RH, 24–359 nm)	0.27 ± 0.10 (mean) 0.07–0.48 (range) (0.12%–0.41% SS, 60–152 nm)	–	This study, all periods

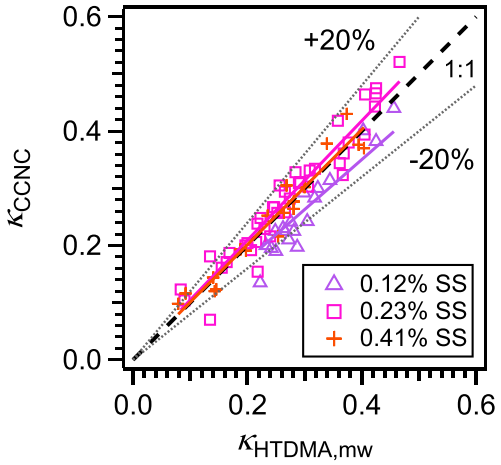

Figure 10. Scatterplot of $\kappa_{HTDMA,mw}$ versus κ_{CCNC} under 0.12%, 0.23%, and 0.41% SS. The solid lines represent the regression lines, which were constrained through the origin. The color of each regression line is the same as that of the markers for the corresponding data points.

g, (c) time-averaged and size-resolved *g*, (d) time- and size-resolved *g*, and (e) time- and size-resolved *g* distributions. The details of the calculation method were described in *Kawana et al.* [2016]. As presented in Figure 11a, the predicted N_{CCN}/N_{CN} somewhat matched the measured values if a single averaged *g* (*g*: 1.33, κ: 0.31) during the observation was applied. However, deviations from the 1:1 line were seen and a large overestimation of N_{CCN} was found at 0.41% SS. The averages of the differences in the ratios of the predicted to the measured N_{CCN}/N_{CN} values from unity at 0.12%, 0.23%, and 0.41% SS (mean relative differences) were from +17% to +36% (Table 4). The RSD values of the ratios of the predicted to the measured N_{CCN}/N_{CN} for three SSs were from 19% to 33%. A larger overestimation with a simplified *g* was seen for smaller particles in the Aitken-mode range, which indicates that the differences in the composition and hygroscopicity of particles in the Aitken- and accumulation-mode ranges needed to be considered. When using the time-resolved but size-averaged *g* (Figure 11b) or size-resolved but time-averaged *g* (Figure 11c), the mean relative differences in the predicted N_{CCN}/N_{CN} from the measured and RSD values were slightly smaller than those when using a single averaged *g*. If the size- and time-resolved *g* (Figure 11d) and size- and time-resolved *g* distribution (Figure 11e) were applied, the mean relative differences (6%–12%) and RSD values (6%–8%) at 0.23% and 0.41% SS were even smaller, and the degrees of overestimation at these SSs improved compared with those in the other cases in Figures 11a–11c. However, for 0.12% SS, the degrees of overestimation were not very different from those in Figures 11a–11c.

One possible reason for the overestimations of the mean relative differences at 0.12% SS could be the presence of sulfate. The larger overestimation and RSD values at 0.12% SS occurred regardless of the inputs from (a) to (e). The large particles, which could activate as CCN at 0.12% SS, had a larger fraction of ammonium sulfate than smaller particles. The hygroscopicity of ammonium sulfate under supersaturated condition was higher than that under subsaturated condition, and the difference was large (~18% in κ value, calculated from *Petters and Kreidenweis* [2007]). Another possible reason could be the uncertainty of the CCN activation diameter. The large particles had large deviations and may have been sensitive to the difference between the predicted and measured activation diameters. These factors might have contributed to the overestimation at 0.12% SS.

The results indicated that the N_{CCN}/N_{CN} of the studied aerosols could be explained well if the variations in the detailed size- and time-resolved *g* (mean relative differences: ≤21%) were considered. This conclusion is similar to that from an urban aerosol study in Nagoya [*Kawana et al.,* 2016]. In the case of the Nagoya aerosols, bimodal hygroscopic distributions with less and more hygroscopic particles were presented and the changes in the relative abundances of particles in the two modes may have affected the N_{CCN}/N_{CN}. For aerosols in the forest at Wakayama, the importance of the variations in the detailed size- and time-resolved *g* was still suggested even though the hygroscopic growth was characterized by unimodal distributions. The presence/absence of new particle formation strongly affected the differences in terms of the hygroscopicity in particle size and periods and must have resulted in the importance of the size- and time-resolved *g* for the CCN prediction.

4.6. Estimating Cloud Droplet Formation and Its Atmospheric Implications

The effects of the hygroscopicity and particle size on cloud droplet activation were assessed using a cloud parcel model with inputs from size-resolved *g* distributions. Although the importance of the hygroscopicity

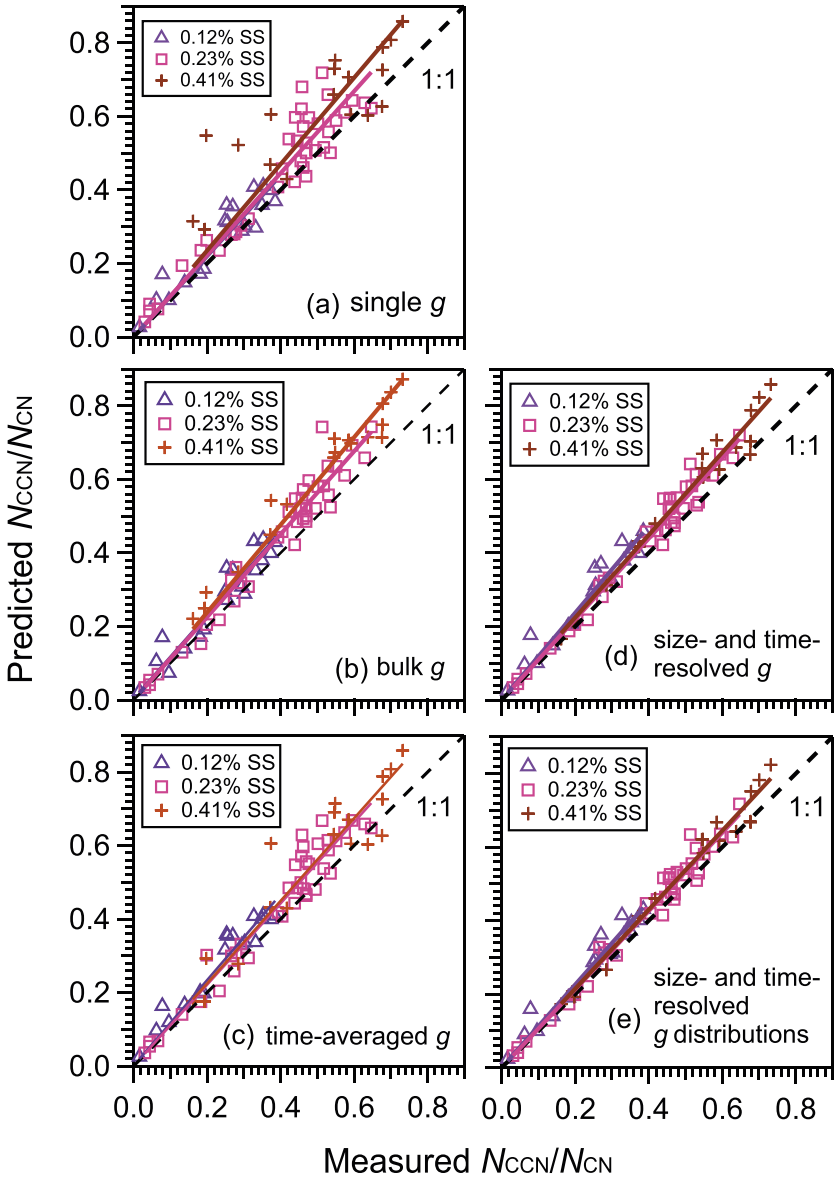

Figure 11. Predicted N_{CCN}/N_{CN} versus the measured N_{CCN}/N_{CN} when considering (a) a single representative g, (b) size-averaged and time-resolved g, (c) time-averaged and size-resolved g, (d) size- and time-resolved g, and (e) size- and time-resolved g distributions. The solid lines represent the regression lines, which were constrained through the origin. The color of each regression line is the same as that of the markers for the corresponding data points.

Table 4. Ratios of the Predicted N_{CCN}/N_{CN} to the Measured N_{CCN}/N_{CN}, With Different Considerations of Particle Hygroscopicity for the Prediction[a]

SS	Single Averaged g	Time-Resolved and Size-Averaged g	Size-Resolved and Time-Averaged g	Size- and Time-Resolved g	Size- and Time-Resolved g Distributions
0.12%	1.21 (0.26)	1.21 (0.26)	1.27 (0.21)	1.27 (0.23)	1.20 (0.21)
0.23%	1.17 (0.19)	1.11 (0.10)	1.12 (0.13)	1.10 (0.07)	1.06 (0.08)
0.41%	1.36 (0.33)	1.24 (0.09)	1.14 (0.16)	1.12 (0.06)	1.07 (0.06)

[a]The values in parentheses are the relative standard deviations of the ratios of the predicted N_{CCN}/N_{CN} to the measured N_{CCN}/N_{CN}.

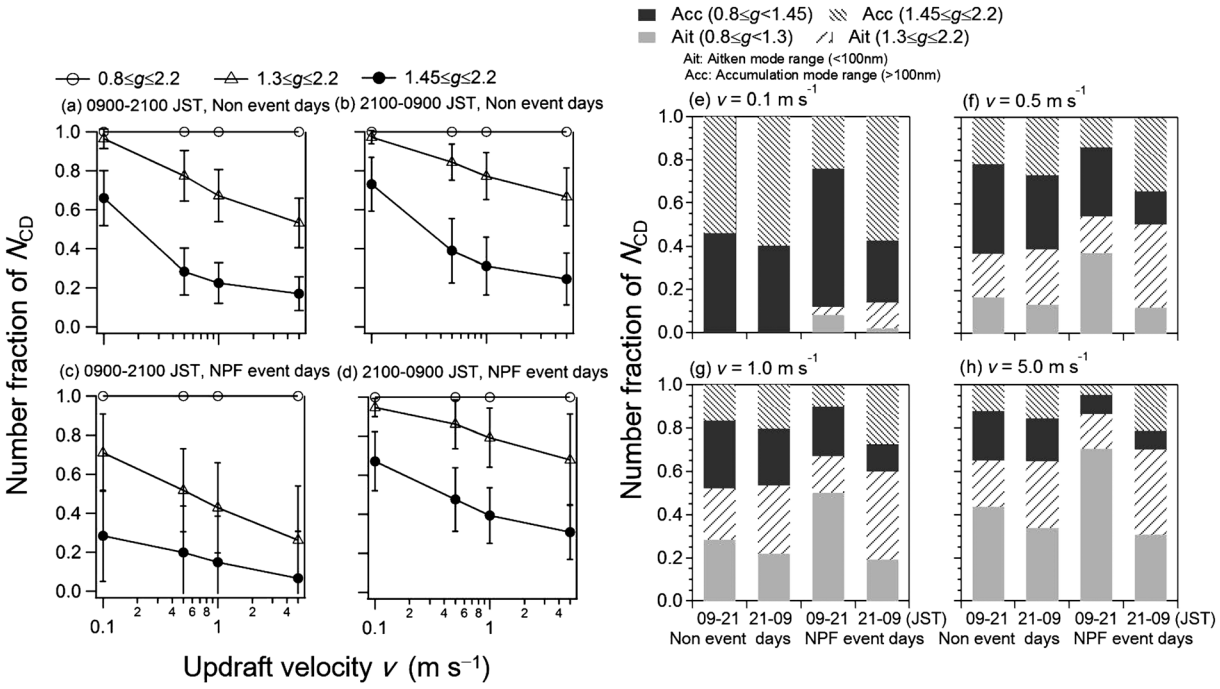

Figure 12. Number fractions of N_{CD} when considering particles in different ranges of g (open triangles: $1.3 \le g \le 2.2$, solid circles: $1.45 \le g \le 2.2$) and those in the base case (open circles: $0.8 \le g \le 2.2$) during (a) 0900–2100 and (b) 2100–0900 JST on nonevent days, and (c) 0900–2100 and (d) 2100–0900 JST on NPF event days. Fractional contributions from particles with different ranges of hygroscopicity and particle size to the total N_{CD} with updraft velocities (v) of (e) 0.1, (f) 0.5, (g) 1.0, and (h) 5.0 m s^{-1}.

of aerosols to cloud droplet formation has been discussed in several studies [*Cubison et al.,* 2008; *Anttila et al.,* 2009], the importance in terms of the mixing state has been assessed in only a few studies [*Anttila*, 2010; *Kawana et al.,* 2014], and they were not conducted in forest environments. The sensitivity analysis results for the contributions from different fractions of particles to N_{CD} are presented in Figures 12a–12d and Table S1 in the supporting information. Whereas the results for all the time sections showed an increasing trend in the contributions from less hygroscopic particles ($g \le 1.3$) and from less and intermediately hygroscopic particles ($g \le 1.45$) as v increased, the absolute values of the contributions markedly depended on the time sections. During 0900–2100 JST on NPF event days (Figure 12c), aerosols in the absence of particles with $0.8 \le g \le 1.3$ induced a 30%–74% decrease in N_{CD} compared to the base case ($0.8 \le g \le 2.2$). The percentages of these decreases were 72%–94% in the absence of particles with $0.8 \le g \le 1.45$. These large percentages indicated the importance of less and intermediately hygroscopic particles to N_{CD} and suggested marked contributions from particles that contain BSOA with low hygroscopicity. In contrast, during 2100–0900 JST on the NPF event days, the absence of particles with $0.8 \le g \le 1.3$ created smaller differences (6%–33%) in N_{CD}. Hence, more hygroscopic particles, which may have included particles in the background air and newly formed particles after aging, were relatively more important. For nonevent days, the results for both 0900–2100 and 2100–0900 JST were similar to the results for 2100–0900 JST on NPF event days. However, the fractions of N_{CD} explained in the absence of less hygroscopic particles and both less and intermediately hygroscopic particles during 0900–2100 JST were smaller on average than those during 2100–0900 JST, which must have also resulted from BSOA formation during the daytime. The effective cloud droplet radii R_{eff} in the base case ($0.8 \le g \le 2.2$) were lower on average than those in the case without less hygroscopic particles with $0.8 \le g \le 1.3$ (or without less and intermediately hygroscopic particles with $0.8 \le g < 1.45$) by 1%–4% (or 3%–9%) at four updraft velocity conditions. The smaller cloud droplets in the presence of particles with low hygroscopicity should have enhanced the cloud albedo and prolonged the lifetime of the cloud droplets and influenced radiative forcing via the indirect effect.

The contributions from particles with different hygroscopicity and particle size to N_{CD} were also assessed in terms of their fractional contributions as presented in Figures 12e–12h and Table S2. Here the sum of the

number concentrations of cloud droplets from four respective groups with different diameters and hygroscopicity ranges was the total N_{CD} in the base with $0.8 \leq g \leq 2.2$. The results showed that cloud droplets mainly formed from particles in the accumulation-mode range at a v of 0.1 m s^{-1}. As v became large, the contributions from smaller particles in the Aitken-mode range and less hygroscopic particles to N_{CD} increased as expected. The contrast between 0900–2100 and 2100–0900 JST on NPF event days was evident, as in the sensitivity analysis; the contribution from less hygroscopic and smaller particles was larger during 0900–2100 JST. In particular, the contribution from less hygroscopic particles ($0.8 \leq g \leq 1.3$) in the Aitken-mode range to N_{CD} averaged more than half (57%) at v values of 1.0 and 5.0 m s^{-1}, which contrasts the cases for nonevent days and during 2100–0900 JST on NPF event days. The contributions from particles with different sizes and hygroscopicity were also assessed based on N_{CCN} at the maximum supersaturations calculated using the cloud parcel model (Figure S6). The tendencies of N_{CCN} against size and periods were similar to those for N_{CD}. These results indicated that the newly formed less hygroscopic particles acted as CCN and contributed substantially to cloud droplet formation under a high updraft velocity.

5. Summary

The size-resolved g distributions at 85% RH and the ratios of CCN to CN at 0.12%, 0.23%, and 0.41% SS were measured for atmospheric aerosols in a forest in Wakayama, Japan. The average size-resolved g distributions at 85% RH had unimodal characteristics. On NPF event days, the size-resolved g distributions and the CCN activation curves were influenced by the formation and growth of new particles and exhibited a clear diurnal pattern. During 0900–2100 JST on NPF event days, less hygroscopic particles ($g \sim 1.1$) appeared in the Aitken-mode range. The g and κ values of the particles were 4%–7% and 27%–40% lower in the Aitken- and accumulation-mode ranges compared to those on nonevent days. The results indicated that the bursts and growth of nanoparticles with fresh, less oxidized, and less hygroscopic newly formed BSOA components occurred, and that the condensation of BSOA components decreased the hygroscopicity of preexisting particles. The g of the particles increased from daytime to nighttime regardless of the particle size. Possible reasons include the aging of particles by oxidation, the production of water-soluble SOA in the aqueous phase, and the inflow of highly hygroscopic components in background aerosols. The d_{act} and N_{CCN} also changed in accordance with the appearance of smaller, less hygroscopic particles during 0900–2100 JST and larger, more hygroscopic particles during 2100–0900 JST; the d_{act} decreased and N_{CCN} increased as the g and κ increased. In contrast, during days without evident NPF events, the g distributions showed similar distributions throughout each day, and the differences with period and particle size were not clear. Monotonous g distributions with more hygroscopic particles suggested that the aerosols were internally mixed, highly oxidized, and aged. The diurnal variations in d_{act} and N_{CCN} were not clear.

The κ values of aerosol particles under subsaturated water vapor conditions ($\kappa_{HTDMA,mw}$) and those under supersaturated conditions (κ_{CCNC}) agreed within 15% on average. This small difference suggests that the effects of organics or less hygroscopic particles, i.e., surface tension reduction and the enhancement of the solute effect, were small. The mean values of κ_{HTDMA} and κ_{CCNC} for particles in the Aitken-mode range during 0900–2100 JST on NPF event days were 0.12 and 0.16, respectively, and the κ_{org} from $\kappa_{HTDMA,mw}$ and κ_{CCNC} was estimated to be 0.12–0.16. The mean values of $\kappa_{HTDMA,mw}$ and κ_{CCNC} during 2100–0900 JST on event days were higher (0.27 and 0.36, respectively). In the CCN closure, the predicted N_{CCN}/N_{CN} values closely matched the measured values if the time- and size-resolved g distributions were applied, which suggests that the differences in g in the particle size and time sections were important to predict N_{CCN}. The assessment of CCN activation and cloud droplet formation showed that less and intermediately hygroscopic particles, which were presumably formed under the strong influence of locally formed BSOA, contributed greatly to N_{CCN} and N_{CD} when v was large. During the nighttime, the more hygroscopic particles in the background air also contributed.

The results from this study provide evidence for the formation of BSOA-rich particles in the Aitken-mode range with respect to particle hygroscopicity and their growth. Moreover, clear diurnal patterns of the hygroscopic growth of newly formed particles in association with the growth of newly formed particles were detected based on the size-resolved g distributions, and the contributions from the newly formed particles to CCN and cloud droplet number concentrations were discussed for the first time based on an observation at a forest site in Asia. The hygroscopicity parameters of the aerosol particles and newly formed BSOA

particles in this Asian forest were obtained under subsaturated and supersaturated water vapor conditions, which should serve as a clue to understanding the properties of biogenic aerosols in different environments and their effects on the climate.

Acknowledgments
We thank the staffs of the Wakayama Research station, Field Science Education and Research Center of Kyoto University, Japan, for the use of the site and their support for the measurements. We acknowledge Y. Iwamoto and Y. Han for their cooperation with the observation and K. Kawamura for the use of instruments. This study was partially supported by JSPS KAKENHI grant JP20671001. The data used for this paper are available freely on request to the corresponding author.

References

Andreae, M. O. (2009), Correlation between cloud condensation nuclei concentration and aerosol optical thickness in remote and polluted regions, *Atmos. Chem. Phys.*, *9*, 543–556, doi:10.5194/acp-9-543-2009.

Andreae, M. O., and D. Rosenfeld (2008), Aerosol-cloud-precipitation interactions. Part I. The nature and sources of cloud-active aerosols, *Earth Sci. Rev.*, *89*, 13–41.

Anttila, T., P. Vaattovaara, M. Komppula, A.-P. Hyvärinen, H. Lihavainen, V.-M. Kerminen, and A. Laaksonen (2009), Size-dependent activation of aerosols into cloud droplets at a subarctic background site during the second Pallas Cloud Experiment (2nd PaCE): method development and data evaluation, *Atmos. Chem. Phys.*, *9*, 4841–4854, doi:10.5194/acp-9-4841-2009.

Anttila, T. (2010), Sensitivity of cloud droplet formation to the numerical treatment of the particle mixing state, *J. Geophys. Res.*, *115*, D21205, doi:10.1029/2010JD013995.

Boy, M., et al. (2004), Overview of the field measurement campaign in Hyytiälä, August 2001 in the framework of the EU project OSOA, *Atmos. Chem. Phys.*, *4*, 657–678, doi:10.5194/acp-4-657-2004.

Cerully, K. M., et al. (2011), Aerosol hygroscopicity and CCN activation kinetics in a boreal forest environment during the 2007 EUCAARI campaign, *Atmos. Chem. Phys.*, *11*, 12,369–12,386, doi:10.5194/acp-11-12369-2011.

Cubison, M. J., B. Ervens, G. Feingold, K. S. Docherty, I. M. Ulbrich, L. Shields, K. Prather, S. Hering, and J. L. Jimenez (2008), The influence of chemical composition and mixing state of Los Angeles urban aerosol on CCN number and cloud properties, *Atmos. Chem. Phys.*, *8*, 5649–5667, doi:10.5194/acp-8-5649-2008.

Dusek, U., G. P. Frank, J. Curtius, F. Drewnick, J. Schneider, A. Kürten, D. Rose, M. O. Andreae, S. Borrmann, and U. Pöschl (2010), Enhanced organic mass fraction and decreased hygroscopicity of cloud condensation nuclei (CCN) during new particle formation events, *Geophys. Res. Lett.*, *37*, L03804, doi:10.1029/2009GL040930.

Ehn, M., T. Petäjä, H. Aufmhoff, P. Aalto, K. Hämeri, F. Arnold, A. Laaksonen, and M. Kulmala (2007), Hygroscopic properties of ultrafine aerosol particles in the boreal forest: Diurnal variation, solubility and the influence of sulfuric acid, *Atmos. Chem. Phys.*, *7*, 211–222, doi:10.5194/acp-7-211-2007.

Engelhart, G. J., A. Asa-Awuku, A. Nenes, and S. N. Pandis (2008), CCN activity and droplet growth kinetics of fresh and aged monoterpene secondary organic aerosol, *Atmos. Chem. Phys.*, *8*, 3937–3949, doi:10.5194/acp-8-3937-2008.

Engelhart, G. J., R. H. Moore, A. Nenes, and S. N. Pandis (2011), Cloud condensation nuclei activity of isoprene secondary organic aerosol, *J. Geophys. Res.*, *116*, D02207, doi:10.1029/2010JD014706.

Facchini, M. C., M. Mircea, S. Fuzzi, and R. J. Charlson (1999), Cloud albedo enhancement by surface-active organic solutes in growing droplets, *Nature*, *401*, 257–259, doi:10.1038/45758.

Facchini, M. C., S. Decesari, M. Mircea, S. Fuzzi, and G. Loglio (2000), Surface tension of atmospheric wet aerosol and cloud/fog droplets in relation to their organic carbon content and chemical composition, *Atmos. Environ.*, *34*, 4853–4857.

Good, N., et al. (2010), Widening the gap between measurement and modelling of secondary organic aerosol properties?, *Atmos. Chem. Phys.*, *10*, 2577–2593, doi:10.5194/acp-10-2577-2010.

Gunthe, S. S., et al. (2009), Cloud condensation nuclei in pristine tropical rainforest air of Amazonia: Size-resolved measurements and modeling of atmospheric aerosol composition and CCN activity, *Atmos. Chem. Phys.*, *9*, 7551–7575, doi:10.5194/acp-9-7551-2009.

Hämeri, K., M. Väkevä, P. P. Aalto, M. Kulmala, E. Swietlicki, J. Zhou, W. Seidl, E. Becker, and C. D. O'dowd (2001), Hygroscopic and CCN properties of aerosol particles in boreal forests, *Tellus*, *53B*, 359–379.

Han, Y., Y. Iwamoto, T. Nakayama, K. Kawamura, T. Hussein, and M. Mochida (2013), Observation of new particle formation over a mid-latitude forest facing the North Pacific, *Atmos. Environ.*, *64*, 77–84.

Han, Y., Y. Iwamoto, T. Nakayama, K. Kawamura, and M. Mochida (2014), Formation and evolution of biogenic secondary organic aerosol over a forest site in Japan, *J. Geophys. Res. Atmos.*, *119*, 259–273, doi:10.1002/2013JD020390.

Hänel, G. (1976), The properties of atmospheric aerosol particles as functions of the relative humidity at thermodynamic equilibrium with the surrounding moist air, *Rev. Geophys.*, *17*, 73–188.

Hennigan, C. J., M. H. Bergin, J. E. Dibb, and R. J. Weber (2008), Enhanced secondary organic aerosol formation due to water uptake by fine particles, *Geophys. Res. Lett.*, *35*, L18801, doi:10.1029/2008GL035046.

Hennigan, C. J., M. H. Bergin, A. G. Russell, A. Nenes, and R. J. Weber (2009), Gas/particle partitioning of water-soluble organic aerosol in Atlanta, *Atmos. Chem. Phys.*, *9*, 3613–3628, doi:10.5194/acp-9-3613-2009.

Hong, J., et al. (2014), Hygroscopicity, CCN and volatility properties of submicron atmospheric aerosol in a boreal forest environment during the summer of 2010, *Atmos. Chem. Phys.*, *14*, 4733–4748, doi:10.5194/acp-14-4733-2014.

Huff Hartz, K. E., T. Rosenørn, S. R. Ferchak, T. M. Raymond, M. Bilde, N. M. Donahue, and S. N. Pandis (2005), Cloud condensation nuclei activation of monoterpene and sesquiterpene secondary organic aerosol, *J. Geophys. Res.*, *110*, D14208, doi:10.1002/2004JD005754.

Irwin, M., N. Robinson, J. D. Allan, H. Coe, and G. McFiggans (2011), Size-resolved aerosol water uptake and cloud condensation nuclei measurements as measured above a Southern Asian rainforest during OP3, *Atmos. Chem. Phys.*, *11*, 11,157–11,174, doi:10.5194/acp-11-11157-2010.

Jung, J., Y. Miyazaki, and K. Kawamura (2013), Different characteristics of new particle formation between urban and deciduous forest sites in Northern Japan during the summers of 2010-2011, *Atmos. Chem. Phys.*, *13*, 51–68, doi:10.5194/acp-13-51-2013.

Kawana, K., N. Kuba, and M. Mochida (2014), Assessment of cloud condensation nucleus activation of urban aerosol particles with different hygroscopicity and the application to the cloud parcel model, *J. Geophys. Res. Atmos.*, *119*, 3352–3371, doi:10.1002/2013JD020827.

Kawana, K., T. Nakayama, and M. Mochida (2016), Hygroscopicity and CCN activity of atmospheric aerosol particles and their relation to organics: Characteristics of urban aerosols in Nagoya, Japan, *J. Geophys. Res. Atmos.*, *121*, 4100–4121, doi:10.1002/2015JD023213.

Kiss, G., E. Tombácz, and H.-C. Hansson (2005), Surface tension effects of humic-like substances in the aqueous extract of tropospheric fine aerosol, *J. Atmos. Chem.*, *50*, 279–294, doi:10.1007/s10874-005-5079-5.

Kristensen, T. B., et al. (2012), Hygroscopic growth and CCN activity of HULIS from different environments, *J. Geophys. Res.*, *117*, D22203, doi:10.1029/2012JD018249.

Kulmala, M., et al. (2001), Overview of the international project on biogenic aerosol formation in the boreal forest (BIOFOR), *Tellus*, *53B*, 324–343.
Kulmala, M., et al. (2004), A new feedback mechanism linking forests, aerosols, and climate, *Atmos. Chem. Phys.*, *4*, 557–562, doi:10.5194/acp-4-557-2004.
Lang-Yona, N., Y. Rudich, T. F. Mentel, A. Buchholz, A. Kiendler-Scharr, E. Kleist, C. Spindler, R. Tillmann, and J. Wildt (2010), The chemical and microphysical properties of secondary organic aerosols from Holm Oak emissions, *Atmos. Chem. Phys.*, *10*, 7253–7265, doi:10.5194/acp-10-7253-2010.
Levin, E. J. T., A. J. Prenni, M. D. Petters, S. M. Kreidenweis, R. C. Sullivan, S. A. Atwood, J. Ortega, P. J. Demott, and J. N. Smith (2012), An annual cycle of size-resolved aerosol hygroscopicity at a forested site in Colorado, *J. Geophys. Res.*, *117*, D06201, doi:10.1029/2011JD016854.
Levin, E. J. T., A. J. Prenni, B. B. Palm, D. A. Day, P. Camouzano-Jost, P. M. Winkler, S. M. Kreidenweis, P. J. Demott, J. L. Jimenez, and J. N. Smith (2014), Size-resolved aerosol composition and its link to hygroscopicity at a forested site in Colorado, *Atmos. Chem. Phys.*, *14*, 2657–2667, doi:10.5194/acp-14-2657-2014.
Martin, S. T., et al. (2010), An overview of the Amazonian Aerosol Characterization Experiment 2008 (AMAZE-08), *Atmos. Chem. Phys.*, *10*, 11,415–11,438, doi:10.5194/acp-10-11415-2010.
Massoli, P., et al. (2010), Relationship between aerosol oxidation level and hygroscopic properties of laboratory generated secondary organic aerosol (SOA) particles, *Geophys. Res. Lett.*, *37*, L24801, doi:10.1029/2010GL045258.
Matsunaga, N. S., T. Mochizuki, T. Ohno, Y. Endo, D. Kusumoto, and A. Tani (2011), Monoterpene and sesquiterpene emissions from Sugi (Cryptomeria japonica) based on a branch enclosure measurements, *Atmos. Pollut. Res.*, *2*, 16–23, doi:10.5094/APR.2011.003.
Matsunaga, N. S., S. Niwa, T. Mochizuki, A. Tani, D. Kusumoto, Y. Utsumi, T. Enoki, and T. Hiura (2013), Seasonal variation in basal emission rates and composition of mono- and sesquiterpenes emitted from dominant conifers in Japan, *Atmos. Environ.*, *69*, 124–130.
McFiggans, G., et al. (2006), The effect of physical and chemical aerosol properties on warm cloud droplet activation, *Atmos. Chem. Phys.*, *6*, 2593–2649, doi:10.5194/acp-6-2593-2006.
Merikanto, J., D. V. Spracklen, G. W. Mann, S. J. Pickering, and K. S. Carslaw (2009), Impact of nucleation on global CCN, *Atmos. Chem. Phys.*, *9*, 8601–8616, doi:10.5194/acp-9-8601-2009.
Miyazaki, Y., J. Jung, P. Fu, Y. Mizoguchi, K. Yamanoi, and K. Kawamura (2012), Evidence of formation of submicrometer water-soluble organic aerosols at a deciduous forest site in northern Japan in summer, *J. Geophys. Res.*, *117*, D19213, doi:10.1029/2012JD018250.
Mochida, M., C. Nishita-Hara, Y. Kitamori, S. G. Aggarwal, K. Kawamura, K. Miura, and A. Takami (2010), Size-segregated measurements of cloud condensation nucleus activity and hygroscopic growth for aerosols at Cape Hedo, Japan, in spring 2008, *J. Geophys. Res.*, *115*, D21207, doi:10.1029/2009JD013216.
Mochida, M., C. Nishita-Hara, H. Furutani, Y. Miyazaki, J. Jung, K. Kawamura, and M. Uematsu (2011), Hygroscopicity and cloud condensation nucleus activity of marine aerosol particles over the western North Pacific, *J. Geophys. Res.*, *116*, D06204, doi:10.1029/2010JD014759.
Mochizuki, T., Y. Endo, S. Matsunaga, J. Chang, Y. Ge, C. Huang, and A. Tani (2011), Factors affecting monoterpene emission from Chamaecyparis obtusa, *Geochem. J.*, *45*, e15–e22.
Okumura, M. (2009), Study on the estimation of the emission flux of the volatile organic compounds based on the forest vegetation (in Japanese), doctoral dissertation, Kyoto Univ., Japan.
Petters, M. D., and S. M. Kreidenweis (2007), A single parameter representation of hygroscopic growth and cloud condensation nucleus activity, *Atmos. Chem. Phys.*, *7*, 1961–1971, doi:10.5194/acp-7-1961-2007.
Pitzer, K. S., and G. Mayorga (1973), Thermodynamics of electrolytes. 2. Activity and osmotic coefficients for strong electrolytes with one or both ions univalent, *J. Phys. Chem.*, *77*, 2300–2308.
Pöschl, U., et al. (2010), Rainforest aerosols as biogenic nuclei of clouds and precipitation in the Amazon, *Science*, *329*, 1513–1516.
Prenni, A. J., M. D. Petters, S. M. Kreidenweis, P. J. DeMott, and P. J. Ziemann (2007), Cloud droplet activation of secondary organic aerosol, *J. Geophys. Res.*, *112*, D10223, doi:10.1029/2006JD007963.
Ramasamy, S., et al. (2016), Total OH reactivity measurement in a BVOC dominated temperate forest during a summer campaign, 2014, *Atmos. Environ.*, *131*, 41–54.
Riipinen, I., et al. (2011), Organic condensation: A vital link connecting aerosol formation to cloud condensation nuclei (CCN) concentrations, *Atmos. Chem. Phys.*, *11*, 3865–3878, doi:10.5194/acp-11-3865-2011.
Rose, D., S. S. Gunthe, E. Mikhailov, G. P. Frank, U. Dusek, M. O. Andreae, and U. Pöschl (2008), Calibration and measurement uncertainties of a continuous-flow cloud condensation nuclei counter(DMT-CCNC): CCN activation of ammonium sulfate and sodium chloride aerosol particles in theory and experiment, *Atmos. Chem. Phys.*, *8*, 1153–1179, doi:10.5194/acp-8-1153-2008.
Sihto, S.-L., et al. (2011), Seasonal variation of CCN concentrations and aerosol activation properties in boreal forest, *Atmos. Chem. Phys.*, *11*, 13,269–13,285, doi:10.5194/acp-11-13269-2011.
Spracklen, D. V., et al. (2008), Contribution of particle formation to global cloud condensation nuclei concentrations, *Geophys. Res. Lett.*, *35*, L06808, doi:10.1029/2007GL033038.
Tang, I. N., and H. R. Munkelwitz (1994), Water activities, densities, and refractive indices of aqueous sulfates and sodium nitrate droplets of atmospheric importance, *J. Geophys. Res.*, *99*, 18,801–18,808, doi:10.1029/94JD01345.
Tani, A., and Y. Kawawata (2008), Isoprene emission from the major native Quercus spp. in Japan, *Atmos Environ.*, *42*, 4540–4550, doi:10.1016/j.atmosenv.2008.01.059.
Topping, D. O., and G. McFiggans (2012), Tight coupling of particle size, number and composition in atmospheric cloud droplet activation, *Atmos. Chem. Phys.*, *12*, 3253–3260, doi:10.5194/acp-12-3253-2012.
Tunved, P., et al. (2006), High natural aerosol loading over boreal forests, *Science*, *312*, 261–263.
VanReken, T. M., N. L. Ng, R. C. Flagan, and J. H. Seinfeld (2005), Cloud condensation nucleus activation properties of biogenic secondary organic aerosol, *J. Geophys. Res.*, *110*, D07206, doi:10.1029/2004JD005465.
Varutbangkul, V., F. J. Brechtel, R. Bahreini, N. L. Ng, M. D. Keywood, J. H. Kroll, R. C. Flagan, J. H. Seinfeld, A. Lee, and A. H. Goldstein (2006), Hygroscopicity of secondary organic aerosols formed by oxidation of cycloalkenes, monoterpenes, sesquiterpenes, and related compounds, *Atmos. Chem. Phys.*, *6*, 2367–2388, doi:10.5194/acp-6-2367-2006.
Vestin, A., J. Rissler, E. Swietlicki, G. P. Frank, and M. O. Andrea (2007), Cloud-nucleating properties of the Amazonia biomass burning aerosol: Cloud condensation nuclei measurements and modeling, *J. Geophys. Res.*, *112*, D14201, doi:10.1029/2006JD008104.
Wang, M., and J. E. Penner (2009), Aerosol indirect forcing in a global model with particle nucleation, *Atmos. Chem. Phys.*, *9*, 236–260, doi:10.5194/acp-9-239-2009.
Wex, H., F. Stratmann, D. Topping, and G. McFiggans (2008), The Kelvin versus the Raoult Term in the Kohler equation, *J. Aerosol Sci.*, *65*, 4004–4016, doi:10.1175/2008JAS2720.1.

Wex, H., M. D. Petters, C. M. Carrico, E. Hallbauer, A. Massling, G. R. McMeeking, L. Poulain, Z. Wu, S. M. Kreidenweis, and F. Stratmann (2009), Towards closing the gap between hygroscopic growth and activation for secondary organic aerosol: Part 1. Evidence from measurements, *Atmos. Chem. Phys.*, *9*, 3987–3997, doi:10.5194/acp-9-3987-2009.

Wu, Z. J., et al. (2013), Relating particle hygroscopicity and CCN activity to chemical composition during the HCCT-2010 field campaign, *Atmos. Chem. Phys.*, *13*, 7983–7996, doi:10.5194/acp-13-7983-2013.

Yu, F., and G. Luo (2009), Simulation of particle size distribution with a global aerosol model: Contribution of nucleation to aerosol and CCN number concentrations, *Atmos. Chem. Phys.*, *9*, 7691–7710, doi:10.5194/acp-9-7691-2009.